



Paleomagnetic field properties at high southern latitude

K. P. Lawrence, L. Tauxe, H. Staudigel, and C. G. Constable

*Scripps Institution of Oceanography, University of California, San Diego, La Jolla, California 92093, USA
(klawrence@ucsd.edu)*

A. Koppers

College of Oceanic and Atmospheric Sciences, Oregon State University, Corvallis, Oregon 97331, USA

W. McIntosh

Earth and Environmental Science Department, New Mexico Institute of Mining and Technology, Socorro, New Mexico 87801, USA

C. L. Johnson

Department of Earth and Ocean Sciences, University of British Columbia, Vancouver, British Columbia V6T 1Z4, Canada

Scripps Institution of Oceanography, University of California, San Diego, La Jolla, California 92093, USA

[1] Statistical analyses of paleomagnetic data from lava flows are used to study geomagnetic field behavior on million year timescales. Previous paleomagnetic studies have lacked high-latitude measurements necessary to investigate the persistence of geomagnetic anomalies observed in the recent and historical field and replicated in some numerical geodynamo simulations. These simulations suggest that reduced convective flow inside the tangent cylinder may affect the magnetic field at high latitude, whereas lower-latitude observations are expressions of columnar/helical flow outside the tangent cylinder. This paper presents new paleointensity and paleodirectional data from 100 volcanic sites in the Erebus Volcanic Province (EVP), Antarctica, and 21 new age determinations by the $^{40}\text{Ar}/^{39}\text{Ar}$ incremental heating method. The new EVP data are combined with previously published paleomagnetic and geochronological results, providing 133 sites, 91 having radioisotopic dates. Modified Thellier-Thellier paleointensity estimates are reported for 47 sites (37 have dates). Ages for the combined data set span 0.03 to 13.42 Ma. The 125 high-quality EVP directional data selected from the merged data set have a non-Fisherian distribution and a mean direction with an inclination anomaly of $\sim 3^\circ$, but 95% confidence limits include the prediction from a geocentric axial dipole. Virtual geomagnetic pole (VGP) dispersions for Brunhes, Matuyama, and the combined 0–5 Ma data set are consistently high compared with values from middle- to low-latitude regions regardless of the criterion used to determine transitional fields. With VGP latitude cut off at 45° , the dispersion ($23.9 \pm 2.1^\circ$) for the combined 0–5 Ma EVP data set is consistent with earlier high-latitude data and paleosecular variation (PSV) in Model G but not with some more recent statistical PSV models. Mean EVP paleointensity of $31.5 \pm 2.4 \mu\text{T}$, derived from 41 high-quality sites, is about half the current value at McMurdo ($\sim 63 \mu\text{T}$). The result is essentially independent of data selection criteria. High VGP dispersion and low-intensity values support the global observation of anticorrelation between directional variability and field strength. Simulations of time-varying dipole strength show that uneven temporal sampling may bias the mean EVP intensity estimate, but the possibility of persistently anomalous field behavior at high latitude cannot be excluded.

Components: 12,615 words, 14 figures, 7 tables.

Keywords: Antarctica; paleointensity; tangent cylinder; paleomagnetism; $^{40}\text{Ar}/^{39}\text{Ar}$.

Index Terms: 1503 Geomagnetism and Paleomagnetism: Archeomagnetism; 1521 Geomagnetism and Paleomagnetism: Paleointensity; 1522 Geomagnetism and Paleomagnetism: Paleomagnetic secular variation.

Received 24 April 2008; **Revised** 2 September 2008; **Accepted** 28 October 2008; **Published** 17 January 2009.

Lawrence, K. P., L. Tauxe, H. Staudigel, C. G. Constable, A. Koppers, W. McIntosh, and C. L. Johnson (2009), Paleomagnetic field properties at high southern latitude, *Geochem. Geophys. Geosyst.*, *10*, Q01005, doi:10.1029/2008GC002072.

1. Introduction

[2] We examine high-latitude paleomagnetic sites in Antarctica to study long-term geomagnetic field behavior near the tangent cylinder, the axisymmetric cylinder tangent to the inner core at the equator that is believed to separate different convective regimes in Earth's outer core (Figure 1). Outside the tangent cylinder, columnar/helical convection dominates as a result of the balance between buoyancy and Coriolis forces. Inside the tangent cylinder the Coriolis forces are weaker leading to reduced convective vigor and less organized three-dimensional flow. These distinct convection regimes have been inferred from recent magnetic field observations [Jackson *et al.*, 2000; Olson and Aurnou, 1999; Wardinski and Holme, 2006], and are identified in modern numerical geodynamo simulations [Sreenivasan and Jones, 2005; 2006; Takahashi *et al.*, 2008]. For a detailed discussion of geodynamo models see Kono and Roberts [2002] and Christensen and Wicht [2007].

[3] Since the late 16th century, direct magnetic measurements (from observatories, surveys, and satellites) have provided steadily improving constraints on spatial and temporal variations of the geomagnetic field (e.g., UFM [Bloxham *et al.*, 1989; Bloxham and Jackson, 1992] and GUFM1 [Jackson *et al.*, 2000]). Such temporally and spatially varying models provide useful constraints on the average field properties over time, the time-averaged field (TAF), and the variation of field properties over time, secular variation. When the time-varying spherical harmonic models like GUFM1 of Jackson *et al.* [2000] are downward continued to the core (assuming an electrically insulating mantle), the field is significantly different from that of a geocentric axial dipole (GAD). This non-GAD structure is inferred to result, in part, from the presence of an inner core, and

differing outer core flow within the tangent cylinder. Of particular interest, in GUFM1, is a persistent low flux region observed over the North Pole, thought to result from the polar vortex convection regime within the tangent cylinder [Hulot *et al.*, 2002; Olson and Aurnou, 1999]. In addition, regions of increased flux (often termed flux lobes) are seen at high northern and southern latitudes near the tangent cylinder [Bloxham *et al.*, 1989; Bloxham and Jackson, 1992; Jackson *et al.*, 2000].

[4] A similar time-varying model of archeomagnetic, sediment, and lava intensities and directions, CALS7K.2, provides analogous constraints on the TAF and paleosecular variation (PSV) for the period from 0 to 7 ka [Korte and Constable, 2005]. Longitudinal structure in CALS7K.2 provides further evidence for flux lobes similar, but damped, to those observed in GUFM1 [Jackson *et al.*, 2000]. This similarity between historical and the 0–7 ka radial field structure suggests a persistence of non-GAD terms resulting from the differing convection regimes on millennial timescales. Our goal is to investigate whether these different convection regimes generate observable differences in properties of the 0–5 Ma paleofield at Earth's surface.

[5] Several data collection efforts have enabled improved temporal and spatial sampling of high-quality paleomagnetic data for the past 5 Ma [see, e.g., Carlot *et al.*, 2000; Herrero-Bervera and Coe, 1999; Herrero-Bervera and Valet, 2005; Holt *et al.*, 1996; Johnson *et al.*, 1998; Laj *et al.*, 2002; Mejia *et al.*, 2005; Miki *et al.*, 1998; Tauxe *et al.*, 2000, 2003, 2004a, 2004b]. One ongoing collaborative effort, the Time-Averaged Field Initiative (TAFI) project, has resulted in new data archived in a comprehensive data set. The TAFI project is providing a significant improvement in the number and quality, as well as temporal and spatial sampling of paleomagnetic data. A summary of the

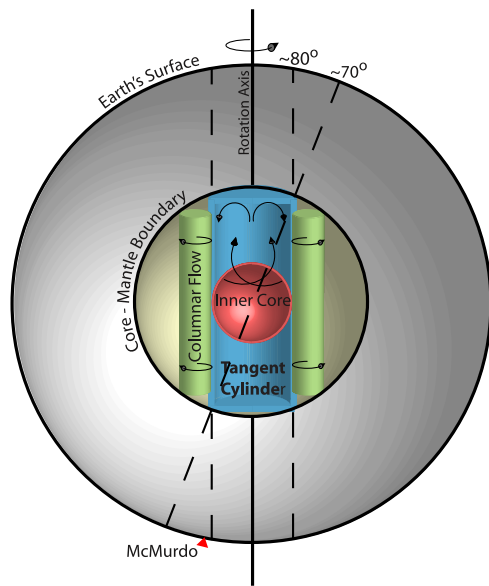


Figure 1. Illustration of outer core flow regimes. The tangent cylinder is denoted by the blue cylinder tangential to the red sphere (inner core). The location of study location (McMurdo) is labeled with a red triangle.

TAFI contributions to date is provided by *Johnson et al.* [2008]. As part of the TAFI project, the Erebus Volcanic Province in Antarctica (Figure 2) provides an excellent opportunity to improve high-

latitude sampling of lava flows suitable for studying the 0–5 Ma TAF and PSV. In particular, this study focuses on Antarctic paleomagnetic directions and intensities measured in a prior study on samples collected in 1965/1966 by *Mankinen and Cox* [1988] and reanalyzed by *Tauxe et al.* [2004a] and those measured from new samples collected in 2003/2004 and 2006/2007 field seasons.

[6] In this paper, we present a brief description of the geological setting and our sampling techniques for the new data. We then discuss paleomagnetic analyses performed on the samples, which yield information about the magnetic field vector at the time of emplacement. We also compare the directional and intensity data from other TAFI sites and compilations of similar quality data from around the world to examine TAF and PSV field properties over the past 5 Ma. We find that the paleointensity results from Antarctica are lower than temporally averaged mean values from the global data set and particularly low when directions lie far from those expected for a dipolar field. Paleomagnetic data cannot be used to provide dynamical constraints on features like the polar vortex but they will provide useful constraints on statistical models for PSV. In conjunction with similar studies on output from numerical dynamo simulations this

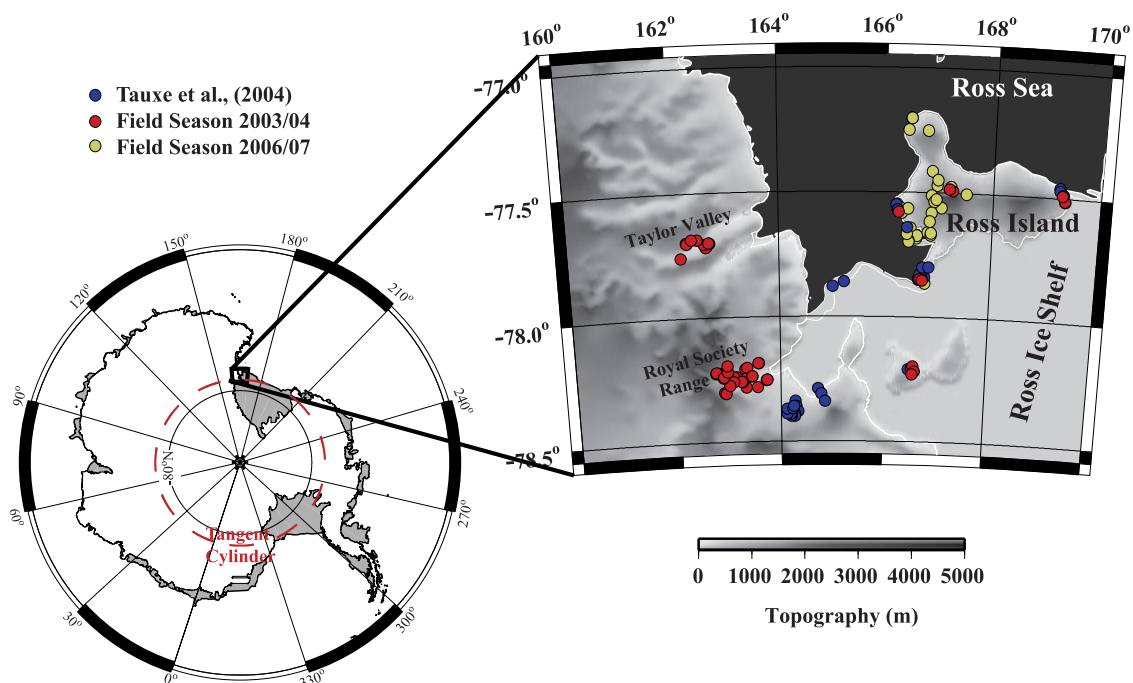


Figure 2. Shaded relief map of the southern portion of the Western Ross Embayment projected as conic equal area and illuminated from N/NW. Red (yellow) circles represent data collected in the 2003/2004 (2006/2007) field season and presented in this study. Blue circles represent data presented by *Tauxe et al.* [2004a]. Small inset is the same projection of the Antarctica continent with the tangent cylinder marked with a red dashed circle ($\sim 79^\circ$).

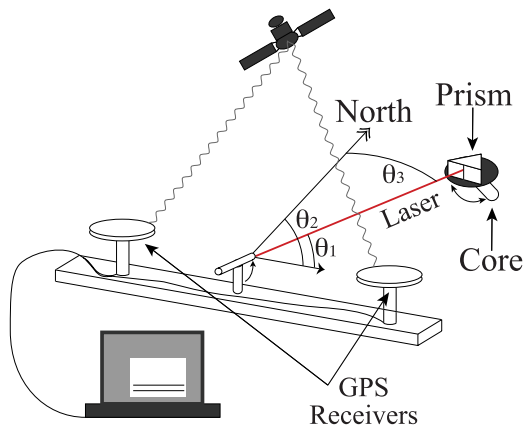


Figure 3. Diagram of differential GPS system for orienting paleomagnetic samples in regions with significant cloud cover. Angles θ_1 and θ_3 are measured in the field, while the orientation in relation to north (θ_2) is determined after data reduction of the GPS location and azimuth.

may lead to future insight about tangent cylinder field dynamics.

2. Study Area

2.1. Geologic Setting

[7] The McMurdo Volcanic Group is a late Cenozoic alkali volcanic province found within the western Ross Embayment [Kyle, 1990a, 1990b], which includes Sheridan Bluff and Mount Early and excludes the Balleny Islands from Harrington's [1958] original designation of the McMurdo Volcanic Group. This group represents the most recent volcanic activity related to the Transantarctic Mountains [Kyle, 1981], from the oldest dated lava from Sheridan Bluff (19.8 Ma) to the youngest and continually erupting Mt. Erebus on Ross Island [Kyle, 1990a]. On the basis of volcanic distribution and tectonic setting, Kyle and Cole [1974] subdivided the McMurdo Volcanic Group into three provinces: Hallett, Melbourne, and Erebus. This study focuses on paleomagnetism and geochronology of basalts from the Erebus Volcanic Province (EVP). Specifically, sites were located on Ross Island, Black Island, within Taylor Valley and in the foothills of the Royal Society Ranges (Figure 2).

[8] The 2006–2007 field season sampled locations restricted to Ross Island, which is home to Mt. Erebus the world's southernmost active volcano. Analysis of Dry Valley Drilling Project (DVDP) cores [Kyle, 1981] shows that Mt. Erebus started erupting at approximately 1.3 Ma, with the oldest

known Mt. Erebus rock having an age of 1.311 Ma [Esser *et al.*, 2004]. Mt. Erebus is still active and is the only volcano in the Southern Hemisphere with a persistent lava lake. In addition to Mt. Erebus, the 2003–2004 field season samples are from locations in the Dry Valleys in and around the Royal Society Range. The Royal Society Range and Dry Valleys are in the Transantarctic Mountains, a 3500 km mountain front that represent the western rift-flank to the West Antarctic Rift System [Fitzgerald, 2002]. Uplift and denudation have exposed Precambrian basement rocks with Late Cenozoic alkaline volcanics and intrusions throughout the region. While this region has undergone various forms of tectonic activity since the Paleozoic, there has been little translation or uplift of crustal blocks since the late Miocene [Cande *et al.*, 2000].

2.2. Sampling

[9] We sampled 70 sites in the Erebus Volcanic Province during the 2003–2004 field season (Figure 2, red circles) and 30 sites during the 2006–2007 field season (Figure 2, yellow circles). Sampling was restricted to lava flows and a few thin dikes because these units typically cool rapidly, essentially recording an instantaneous geomagnetic field at the time and location of emplacement. Sites exhibiting evidence of postemplacement tilting (e.g., slumping or faulting) were not sampled. To minimize the necessity for additional $^{40}\text{Ar}/^{39}\text{Ar}$ dates, site locations were chosen based on previous geochronological studies by Wilch [1991] and Wilch *et al.* [1993], who provided radioisotopic dates for many lava flows in the EVP. At each field site, a minimum of 10 standard 2.5 cm diameter samples were drilled using a gasoline powered drill with a mixture of water and glycol for the drilling fluid. The samples were oriented using at least two of three methods; magnetic compass, sun compass, and/or a differential Global Positioning System (GPS) orientation technique.

[10] We developed the differential GPS technique (see Figure 3) at Scripps Institution of Oceanography to facilitate sample orientation at high latitude where weather conditions often preclude the use of a sun compass. This method uses two Novotel GPS receivers attached to either end of a 1-m nonmagnetic base. The location and azimuth of the horizontal baseline are computed from the difference in signals detected by the two receivers. The orientation of the baseline is transferred to the paleomagnetic samples with a rotatable laser mounted on the base. A prism attached to the sample orientation

device reflects the laser beam back to an observer at the laser, allowing accurate orientation of the drill core with respect to the differential GPS baseline. The orientations derived by the differential GPS are nearly identical to those obtained by a sun compass with 0.6° average and 2.5° maximum deviation, respectively. Drawbacks of the method include an additional ~ 5 min to orient each sample and bulkier equipment to transport. Nonetheless, achieving sun compass accuracy in orientations when direct sunlight is not readily available is a major breakthrough for high-latitude paleomagnetic field studies.

2.3. Previous Work in the Mt. Erebus Volcanic Province

[11] *Mankinen and Cox* [1988] completed a paleomagnetic study of 303 fully oriented samples from 39 lava flows from the Erebus Volcanic Province in the vicinity of McMurdo Sound in 1965 and 1966 using a gasoline powered drill for sample collection. Oriented block samples were taken from an additional 11 lava flows. They reported site means based on the natural remanent magnetizations (NRMs). The approximate locations of the sites are shown as blue circles in Figure 2. *Tauxe et al.* [2004a] remeasured all the NRM directions and subjected at least five separately oriented specimens from every site to stepwise alternating field or thermal demagnetization. They also selected approximately 100 specimens based on the specimen's high median demagnetizing fields for a *Thellier and Thellier* [1959] type experiment. Of the 36 sites that *Tauxe et al.* [2004a] observed with reliable directions, 16 sites have both direction and paleointensity estimates. That study also provided new $^{40}\text{Ar}/^{39}\text{Ar}$ dates for nine sites, ranging from 0.28 to 1.49 Ma. Because *Mankinen and Cox* [1988] focused on Brunhes-aged lava flows, only seven sites are of reverse polarity. The new study presented here aims to expand the age distribution and polarity sampling of the Antarctic region and to contribute many more paleointensity estimates.

[12] *Baraldo et al.* [2003] reported additional paleomagnetic directions from 21 sites dated at 153 ± 46 ka from Deception Island, Antarctica (63°S , 60.6°W). These have a mean direction with a Fisherian distribution and virtual geomagnetic pole (VGP) dispersion compatible with current paleosecular variation models. Unfortunately, no intensities were measured, and the sample ages are ill constrained, so these measurements are not included in this study.

[13] *Jovane et al.* [2008] presented a paleomagnetic analysis of a 16 m piston sedimentary core (Eltanin 27–21) located in the Ross Sea (69.03°S , 179.83°E). Using variation in the inclinations during stable polarity intervals they report a virtual geomagnetic pole dispersion over the past 2 Ma of $30.3^\circ \pm 4.3^\circ$. *Roberts et al.* [2007] published a study of a high-resolution early Miocene polarity transition record for two glacial marine sediments cores (CRP-2 and CRP-2/2A) in McMurdo Sound. Although *Roberts et al.* [2007] do not publish dispersion results they argue that the consistency of vigorous inclination changes between the two cores indicates dynamic field behavior during transition rather than a smooth transition with longitudinally confined VGP paths. Six sediment cores spanning 0 to 780 ka from the Wilkes Land Basin (adjacent to the Erebus Volcanic Province) provide paleomagnetic inclination and relative paleointensity, exhibiting geomagnetic excursions with oscillations to shallow inclinations but never negative inclination [*Macri et al.*, 2005; *Macri et al.*, 2006].

3. Paleomagnetic Methods and Results

[14] Fundamental paleomagnetic observations are declination (D), inclination (I), and intensity ($|B|$), where

$$\begin{aligned} D &= \tan^{-1} \left(\frac{B_y}{B_x} \right), \\ I &= \tan^{-1} \left(\frac{B_z}{(B_x^2 + B_y^2)^{1/2}} \right), \\ |B| &= (B_x^2 + B_y^2 + B_z^2)^{1/2}, \end{aligned} \quad (1)$$

and B_x , B_y , B_z are the vector components of the magnetic field expressed in a local geographic coordinate system at any given location. In sections 3.2 and 3.3 we present the directional and intensity experimental methods and associated results, respectively. In each section we characterize the mean values for the fundamental observations as well as the statistics describing the variation of the paleofield in both time and space.

3.1. Hysteresis

[15] A selection of eight representative specimens were chosen for hysteresis experiments (see examples in Figure 4). These exhibited a range of behaviors from “goose-necked” (Figures 4a and 4d), wasp-waisting (Figures 4b and 4e), to more

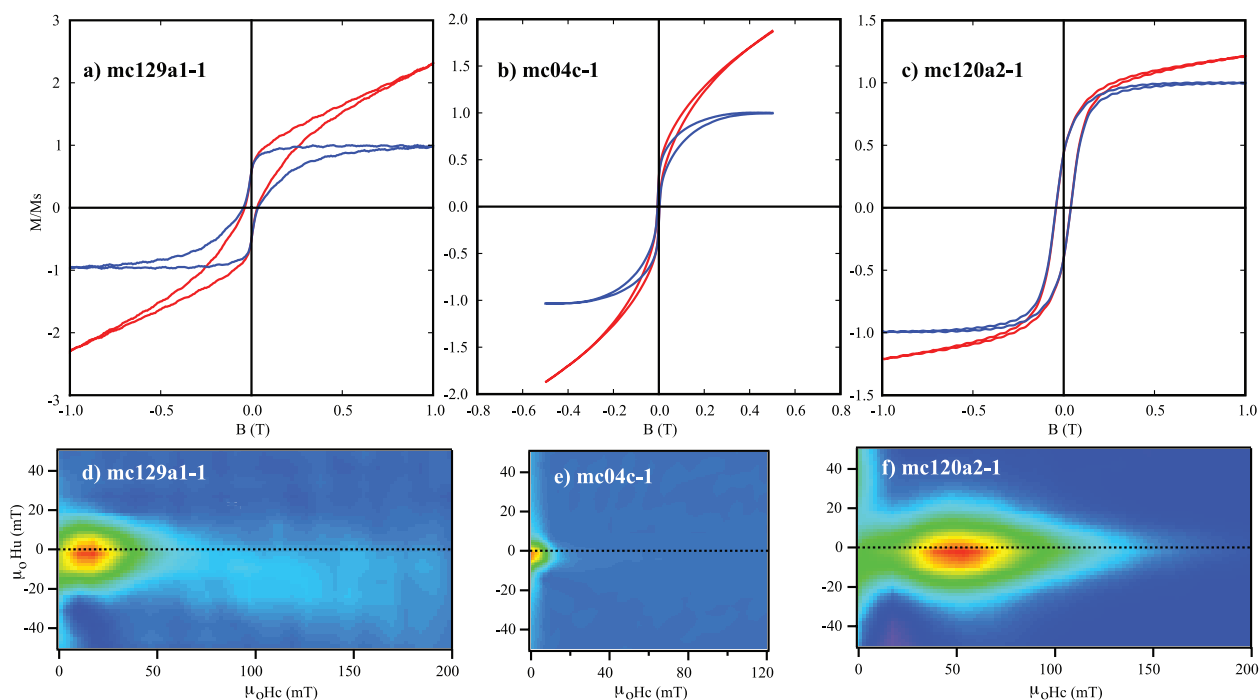


Figure 4. (a–c) Representative hysteresis loops and (d–f) FORC diagrams. All FORCs were processed using the FORCinel code of *Harrison and Feinberg* [2008].

typical “pseudo-single domain” behavior (Figures 4c and 4f). The goose-necked hysteresis loops are likely associated with mixtures of hematite and magnetite mineralogies, while the wasp-waisted loops are typical of single-domain/superparamagnetic assemblages [Tauxe *et al.*, 1996].

3.2. Paleodirections

[16] We measured NRM directions for all specimens using a 2G cryogenic magnetometer or a Molspin “Minispin” magnetometer if the NRM exceeded $7.5 \times 10^{-5} \text{ Am}^2$. At least five specimens per site (784 specimens in total) were magnetically cleaned using either stepwise alternating field (AF) (461 specimens) or thermal demagnetization (323 specimens). Most sites were treated using both techniques using either the Sapphire Instruments SI-4 uniaxial AF demagnetizer or SIO home-built ovens with 2°C accuracy.

[17] For the AF demagnetization experiments, we measured samples at the following applied field magnitudes: 5, 10, 15, 20, 30, 40, 50, 60, 80, 100, 120, 150, and 180 mT. At peak fields of 100 mT and higher, the specimens were subjected to a “triple demagnetization” protocol [Stephenson, 1993] whereby specimens were demagnetized along all three axes, measured and then demagnetized along the *y* axis, measured and then demag-

netized along the *z* axis. At every demagnetization field strength, an average of the three measurements was calculated to counteract the effect of (rarely observed) gyroremanent magnetization, an unwanted remanence produced during demagnetization due to preferential anisotropic orientation in the easy axes of magnetization. During the AF demagnetization procedure, specimen orientations alternated from positive to negative axes with each field step. If the difference in directions between field steps was more than 5° a “double demagnetization” protocol [Tauxe *et al.*, 2003, 2004a] was implemented to detect possible acquisition of anhysteretic remanence.

[18] Thermal demagnetization steps of 50°C were used from 150° to 500°C, steps of 25°C were used from 520° to 560°C, and steps of 5–10°C were used when necessary until the maximum unblocking temperature was reached. One site with an unusual magnetic remanence spectrum, mc164, required 50°C steps to 620°C and 5°C from 620 to 650°C. Specimens from this site were subjected to a hysteresis and FORC experiment and behaved in a manner similar to that shown in Figures 4a and 4d, suggesting a hematite dominated mineralogy. Most thermal demagnetization experiments were performed in conjunction with an IZZI modified Thellier-Thellier experiment [Tauxe and Staudigel,

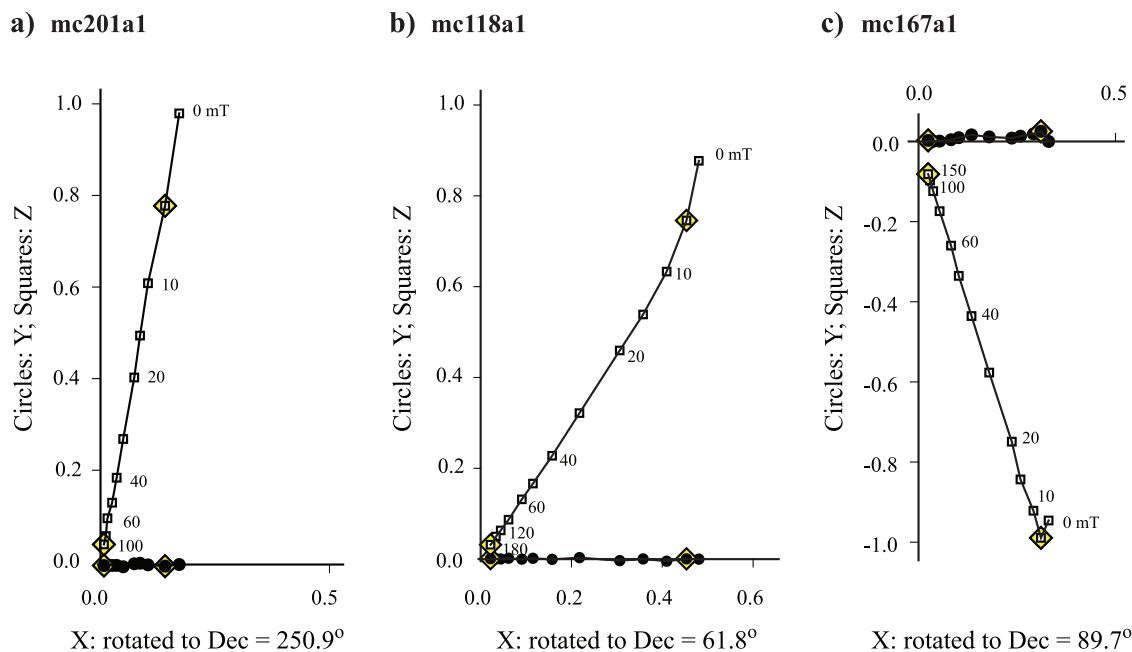


Figure 5. Vector-endpoint diagrams of AF (alternating field) demagnetization experiments for representative specimens, (a) mc201a1, NRM is normalized to $1.84 \times 10^{-5} \text{ Am}^2$, (b) mc118a1, NRM is normalized to $3.53 \times 10^{-5} \text{ Am}^2$, (c) mc167a1, NRM is normalized to $6.78 \times 10^{-5} \text{ Am}^2$. Closed (open) circles are the horizontal (vertical) plane projection of the directional vector. The x-direction has been rotated to the NRM declination (labeled for each specimen). The yellow diamonds represent the maximum and minimum demagnetization steps used in the principal component analysis.

2004; Yu *et al.*, 2004] to obtain paleointensity information (see section 3.3).

[19] As with the data analyzed by Tauxe *et al.* [2004a], the Antarctic specimens are very well-behaved. With few exceptions, the magnetization of specimens treated with AF decayed linearly to the origin. Some thermally demagnetized specimens experienced significant alteration, but we attribute this in part to the Thellier-Thellier experimental method, in which the samples are heated repeatedly and alteration can occur in the presence of an external magnetic field. Representative AF and thermal demagnetization data are plotted on vector end-point diagrams in Figures 5 and 6. Principal component analysis [Kirschvink, 1980] was used to determine characteristic directions or best fit planes through the demagnetization data.

We were unable to determine principal component directions or best fit planes for three sites (mc151, mc149, and mc159); these sites were excluded from the data compilation. Specimens that yielded aberrant behavior were tested for rotational errors that could have occurred during sample collection, while cutting, or measuring the magnetic direction. If these specimens failed the rotational test or showed evidence of mismarked direction (24 samples from the new collections and 3 from the collection of Mankinen and Cox [1988]), the results were not included. Figure 7 shows an example of a test for mismarked drill direction, where the paleomagnetic direction (in geographic coordinates) of mc133g (black circle) is plotted with directions of other samples from the same site (red circles). The azimuth direction of mc133g is

Figure 6. Arai plot of NRM remaining versus pTRM gained during an IZZI-modified T-T paleointensity experiment for representative specimens, (a) mc217b1, NRM is normalized to $1.06 \times 10^{-4} \text{ Am}^2$, (b) mc120b1, NRM is normalized to $4.13 \times 10^{-5} \text{ Am}^2$, (c) mc147k2, NRM is normalized to $3.62 \times 10^{-5} \text{ Am}^2$, and (d) mc131e1, NRM is normalized to $1.98 \times 10^{-5} \text{ Am}^2$. Open (closed) circles represent the ZI (IZ) steps of the heating sequence (see text). The green line represents the inferred paleointensity and pTRM checks are shown as blue triangles. Inset is a vector-endpoint diagram of direction during thermal demagnetization (the zero-field only steps of the T-T experiment) where the x-direction has been rotated to the NRM declination (labeled for each specimen). Closed circles are the horizontal plane and open circles are the vertical plane. The yellow diamonds represent the maximum and minimum demagnetization steps used in the principal component analysis.

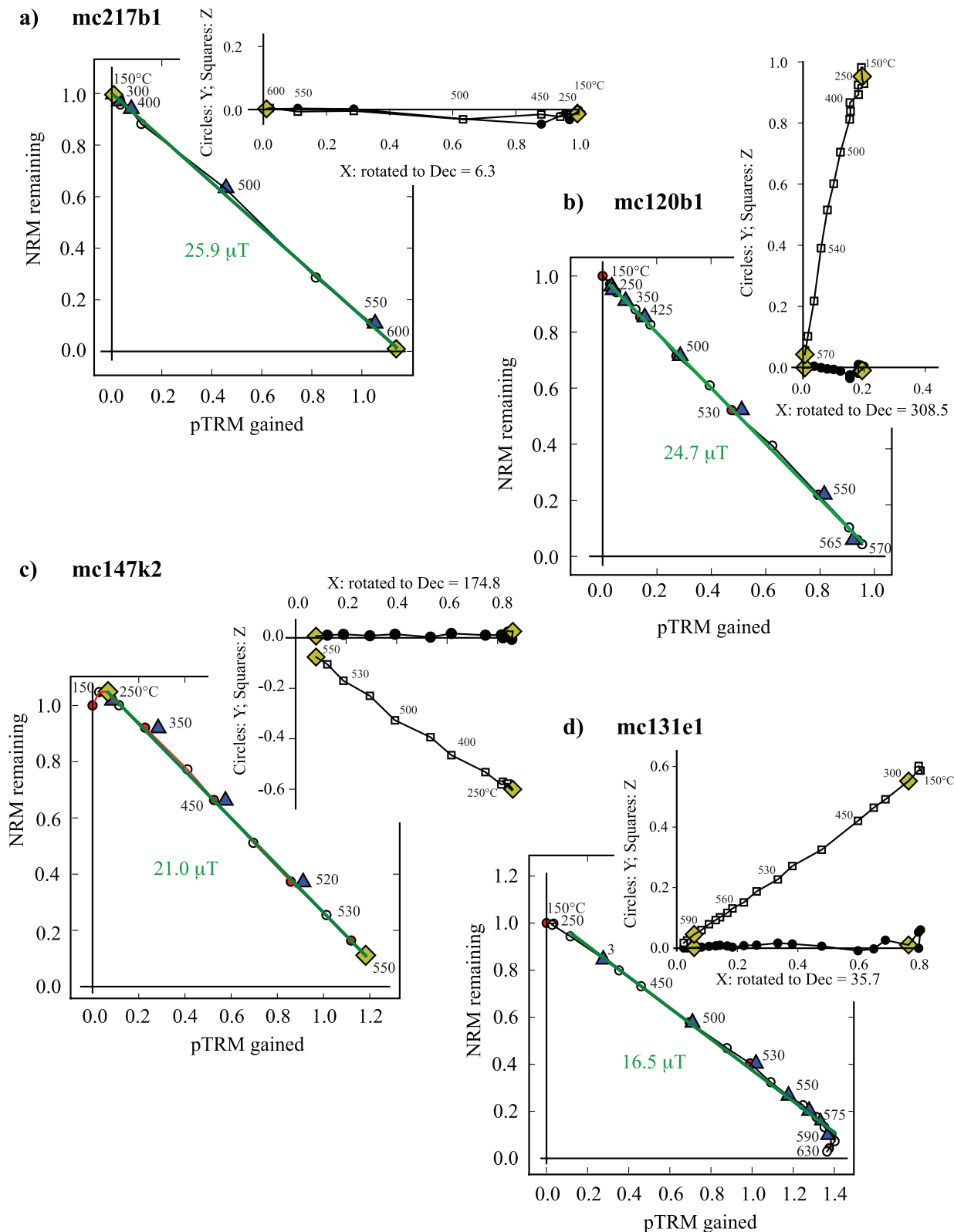


Figure 6

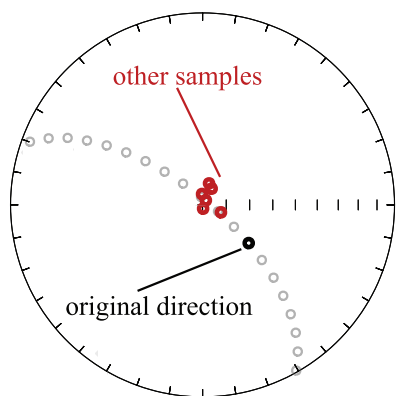


Figure 7. Test for mismatched drill direction of sample mc133g. The original direction for mc133g (black circle) is plotted with directions from other samples of the same site (red circles). Rotation of the azimuth about the drill direction in steps of 10° (gray circles). Mc133g was mismatched by rotation about the drill direction of $\sim 20^\circ$.

rotated in 10° steps (gray circles) about the axis of the drill direction, showing that a rotation of $\sim 20^\circ$ aligns sample mc133g with other samples of the same site. This can happen if samples break off in the hole prior to orientation, or a stray mark is misinterpreted as the brass orientation mark. Therefore, we conclude mc133g was misoriented and does not provide an accurate record of direction for this site.

[20] Site mean directions are calculated using characteristic directions for experiments with at least four consecutive demagnetization steps, directions trending to the origin, and a maximum angle of deviation (MAD) less than 5° . Some demagnetization data were better interpreted as best fit planes, as opposed to lines and these were included if their MADs were less than 5° based on at least four consecutive demagnetization steps. We used Fisher statistics [Fisher, 1953] for sites with only directional data and the method of McFadden and McElhinny [1988] for combining lines and planes for those sites with best fit planes. A summary of site locations and mean directions is presented in Table 1 and plotted in Figure 8a. Our measure of data quality for individual sites is based on $k = (N - 1)/(N - R)$, where N is the number of data and R is the length of the resultant vector. Guided by results from Johnson *et al.* [2008] we define data selection criteria for further analyses as $n \geq 5$ and $k > 50$. All sites had k values greater than 50 and α_{95} values less than 10° . There are 8 sites (mc106, mc110, mc112, mc113, mc122, mc124, mc130, mc134) that are excluded because they are

older than 5 Ma. This yields 89 new sites with high-quality directional data with ages from 0 to 5 Ma. With the inclusion of 36 sites from Tauxe *et al.* [2004a] with ages ranging from 0 to 5 Ma that meet the above criteria, the following analysis incorporates 125 Antarctic sites. The mean directions of normal, reverse, and combined polarity data are shown in Figure 8b and tabulated in Table 2.

[21] The virtual geomagnetic pole (VGP) is the pole position of the equivalent geocentric dipole that would give rise to the observed magnetic field direction at any given place. Transitional data are often defined as measurements with absolute value of VGP latitude (λ_{VGP}) less than 45° and are often excluded from estimates of PSV and the TAF. However, an arbitrary VGP latitude cutoff may bias the interpretation of PSV and TAF properties [Clement, 2000; Coe *et al.*, 2000]. For this reason, we present results with (1) no λ_{VGP} cutoff, (2) a cutoff of $|\lambda_{VGP}| < 45^\circ$, and (3) an iteratively defined λ_{VGP} (37° for this data set) that is empirically derived from dispersion, as proposed by Vandamme [1994]. VGP directions with ages less than 5 Ma are shown in Figure 8c, with corresponding λ_{VGP} cutoffs.

[22] Inclination anomaly (ΔI) is a summary statistic of average direction often used to describe the TAF, and is defined as:

$$\Delta I = I_{obs} - I_{GAD} \quad (2)$$

where I_{obs} is the observed site inclination and I_{GAD} is the prediction of the geocentric axial dipole field. PSV is often represented by S_B , the root mean square angular deviation of VGPs about the geographic axis,

$$S_B = \sqrt{\frac{1}{N-1} \sum_{i=1}^N \left(\Delta_i^2 - \frac{S_{w_i}^2}{N_{s_i}} \right)} \quad (3)$$

where Δ_i represents the angular deviation of the pole for the i th site from the geographic North Pole, N is the number of sites, and S_B represents the geomagnetic signal remaining after correcting for the within-site VGP dispersion, S_{w_i} ($81^\circ/\sqrt{k}$), determined from N_{s_i} samples. Here, k has been converted to an approximation for the precision parameter for VGPs using the transformation provided by Creer [1962]. A summary of dispersion and inclination anomaly as a function of λ_{VGP} cutoff can be found in Table 3 where the 95% confidence limits are calculated using a bootstrap technique.

Table 1. Average Directions by Site^a

Site	Site Latitude (°N)	Site Longitude (°E)	Dec	Inc	N	<i>k</i>	α_{95}	VGP Lat	VGP Lon	Pol	Preferred Age (Ma \pm 2 σ)	Age Reference
mc100	-78.302	162.900	9.9	-76.6	7	582.7	2.6	75.9	180.6	N	0.86 \pm 0.23	This study
mc101	-78.306	162.928	38.5	-80.6	6	460.8	3.1	78.4	239.0	N	1.07 \pm 0.01	Wilch [1991]
mc102	-78.235	163.352	155.3	75.6	8	245.9	3.6	-72.8	303.0	R	0.26 \pm 0.02	Wilch [1991]
mc103	-78.235	163.360	138.6	72.9	7	833.3	2.1	-66.1	284.7	R	1.42 \pm 0.03	Wilch [1991]
mc104	-78.238	163.401	72.1	-77.2	7	367.4	3.2	66.5	262.2	N	0.29 \pm 0.02	This study
mc105	-78.245	163.231	192.1	69.5	8	755.0	2.0	-64.6	0.2	R	0.86 \pm 0.07	Armstrong [1978]
mc106	-78.210	163.308	19.5	-76.7	5	410.8	3.8	75.3	197.5	N	13.42 \pm 0.18	This study
mc107	-78.204	163.347	96.0	-84.8	7	1007.6	2.0	73.6	304.3	N	2.57 \pm 0.38	Wilch [1991]
mc108	-78.247	163.323	69.8	-72.4	5	403.2	3.8	59.8	252.3	N	0.41 \pm 0.14	This study
mc109	-78.282	163.544	174.6	75.4	6	477.4	3.1	-74.1	334.4	R	1.26 \pm 0.04	Wilch [1991]
mc110	-78.238	163.443	253.5	79.6	5	218.2	5.2	-69.9	89.6	R	7.94 \pm 0.24	Wilch [1991]
mc111	-78.224	162.787	47.9	-67.6	7	1243.3	1.7	57.4	223.9	N	1.99 \pm 0.04	This study
mc112	-78.238	163.441	232.9	75.7	5	220.9	5.2	-68.1	60.0	R	7.63 \pm 0.32	Wilch [1991]
mc113	-78.226	162.735	264.4	75.4	6	504.1	3.0	-61.3	89.3	R	6.73 \pm 0.17	Wilch [1991]
mc114	-78.224	162.783	52.4	-69.7	5	614.0	3.1	59.4	230.7	N	1.62 \pm 0.28	Wilch [1991]
mc115	-78.243	162.958	77.7	68.1	6	359.2	3.5	-47.4	227.7	R	2.46 \pm 0.31	This study
mc116	-78.222	162.744	274.6	-81.2	5	139.7	6.5	70.0	42.5	N	1.14 \pm 0.11	Wilch [1991]
mc117	-78.235	162.973	164.5	70.0	6	3152.4	1.2	-65.1	321.0	R	2.28 \pm 0.24	Wilch [1991]
mc118	-78.241	163.141	58.9	-53.1	7	99.0	6.1	39.1	229.8	N	0.31 \pm 0.04	This study
mc119	-78.239	162.957	124.8	49.0	6	864.8	2.3	-36.1	281.2	R	1.08 \pm 0.22	Wilch [1991]
mc120	-78.241	163.092	73.6	-70.6	9	509.6	2.3	56.5	253.9	N	1.76 \pm 0.05	Wilch [1991]
mc121	-78.235	162.954	117.4	78.4	11	389.2	2.3	-70.3	250.0	R	2.51 \pm 0.06	Wilch [1991]
mc122	-78.187	163.580	12.2	-72.4	5	177.8	5.8	69.0	182.0	N	12.70 \pm 0.09	This study
mc123	-78.254	163.729	76.1	-82.1	8	317.2	3.1	73.0	280.9	N	1.93 \pm 0.05	This study
mc124	-78.186	163.567	13.2	-73.4	7	654.8	2.4	70.5	184.1	N	12.61 \pm 0.11	This study
mc125	-78.254	163.730	344.1	-67.7	9	93.1	5.4	61.8	142.2	N	4.26 \pm 0.18	Wilch [1991]
mc126	-78.253	163.737	4.2	-78.0	8	294.6	3.2	78.7	172.1	N		
mc127	-78.254	163.733	326.2	-67.2	8	666.9	2.1	59.1	119.5	N	1.94 \pm 0.07	Wilch [1991]
mc128	-78.210	166.571	36.9	-80.1	8	395.8	2.8	78.0	238.4	N		
mc129	-78.214	166.577	22.1	-54.5	9	490.9	2.3	45.8	192.8	N		
mc130	-78.210	166.579	150.5	46.1	6	405.9	3.3	-37.5	313.1	R	7.25 \pm 0.07	This study
mc131	-78.214	166.573	22.3	-58.1	8	526.8	2.4	49.5	193.7	N		
mc132	-78.206	166.552	6.3	38.3	6	195.4	5.0	-9.8	172.5	R		
mc133	-78.199	166.584	36.3	-85.7	6	235.0	4.4	83.0	300.6	N		
mc134	-78.219	166.607	12.5	-84.3	5	886.4	2.6	87.5	273.8	N	9.02 \pm 0.05	This study
mc135	-78.231	166.565	264.1	-77.8	8	215.3	3.8	62.9	46.7	N		
mc136	-78.282	163.329	102.2	18.0	6	334.6	3.7	-11.5	263.4	R	1.99 \pm 0.60	Wilch [1991]
mc137	-78.261	163.257	71.2	34.2	5	120.4	8.7	-14.7	231.1	R		
mc138	-78.260	163.240	83.0	12.1	5	473.2	4.4	-4.6	245.1	R	1.21 \pm 0.18	Wilch [1991]
mc139	-78.260	163.080	168.6	79.0	5	1124.5	2.3	-80.0	318.7	R	0.88 \pm 0.08	This study
mc140	-78.276	163.004	343.7	-79.2	7	654.7	2.4	79.8	128.4	N	2.03 \pm 0.09	This study
mc141	-77.580	166.246	133.0	83.5	7	549.9	2.6	-80.0	235.4	R	1.31 \pm 0.02	Wilch [1991]
mc142	-77.851	166.680	311.9	84.7	10	585.0	2.0	-69.3	144.1	R	1.23 \pm 0.02	This study
mc143	-78.244	162.879	30.3	-46.9	7	122.6	5.5	38.1	197.3	N	2.08 \pm 0.65	This study
mc144	-77.850	166.688	194.4	79.9	8	195.5	4.0	-81.6	21.6	R		
mc145	-78.240	162.893	28.6	2.7	6	378.0	3.5	9.0	191.9	N	1.90 \pm 0.12	Wilch [1991]
mc146	-78.220	162.963	236.3	62.0	7	117.8	5.6	-48.9	50.1	R	1.37 \pm 0.42	Wilch [1991]
mc147	-78.196	162.962	220.2	67.4	5	830.9	2.7	-58.5	35.1	R	1.63 \pm 0.34	Wilch [1991]
mc148	-77.492	167.249	282.1	-80.2	6	140.6	5.7	69.6	53.9	N	0.72 \pm 0.66	Wilch [1991]
mc150	-77.714	162.637	253.5	84.3	5	125.5	6.9	-75.9	112.1	R	3.57 \pm 0.14	Wilch et al. [1993]
mc152	-77.716	162.645	327.2	-85.3	6	1325.5	1.9	83.3	31.5	N	3.87 \pm 0.15	Wilch et al. [1993]
mc153	-77.760	162.144	315.9	58.4	7	109.7	5.8	-29.9	123.6	R	2.53 \pm 0.13	Wilch et al. [1993]
mc154	-77.719	162.626	297.9	87.1	5	429.1	3.7	-74.2	143.6	R	2.19 \pm 0.08	Wilch et al. [1993]
mc155	-77.699	162.253	226.2	77.7	8	221.3	3.7	-72.7	57.7	R	1.50 \pm 0.05	Wilch et al. [1993]
mc156	-77.705	162.592	161.3	71.1	5	340.9	4.2	-66.9	315.0	R	1.89 \pm 0.13	Wilch et al. [1993]
mc157	-77.703	162.264	263.3	70.5	8	82.3	6.2	-54.3	82.9	R		
mc158	-77.688	162.462	46.9	43.2	6	555.8	2.9	-16.5	206.0	R	3.74 \pm 0.25	Wilch et al. [1993]
mc160	-77.687	162.354	227.9	76.2	10	227.7	3.2	-70.0	55.8	R	3.47 \pm 0.05	Wilch et al. [1993]
mc161	-77.702	162.694	171.3	55.1	6	281.0	4.1	-47.8	332.2	R		
mc162	-77.701	162.690	174.6	58.1	7	270.7	3.8	-51.0	336.0	R	2.56 \pm 0.13	Wilch et al. [1993]

Table 1. (continued)

Site	Site Latitude (°N)	Site Longitude (°E)	Dec	Inc	N	<i>k</i>	α_{95}	VGP Lat	VGP Lon	Pol	Preferred Age (Ma $\pm 2\sigma$)	Age Reference
mc163	-77.700	162.680	175.6	51.5	6	261.2	4.2	-44.4	337.5	R		
mc164	-77.514	169.330	199.9	86.1	10	1912.3	1.1	-84.2	142.3	R	1.36 \pm 0.01	This study
mc165	-77.513	169.332	141.9	81.8	8	174.1	4.2	-80.2	261.0	R	1.45 \pm 0.06	This study
mc166	-77.849	166.670	224.9	73.8	8	634.1	2.2	-67.0	51.6	R	1.33 \pm 0.12	This study
mc167	-77.487	169.294	179.7	74.5	9	82.1	5.7	-73.5	348.8	R		
mc168	-77.488	169.292	187.3	68.2	7	398.3	3.0	-63.7	359.6	R	1.38 \pm 0.05	This study
mc170	-77.854	166.714	2.7	-87.2	5	7835.9	0.9	83.4	344.4	N	1.03 \pm 0.10	This study
mc200	-77.550	166.161	296.8	-83.7	5	389.6	3.9	77.0	45.2	N	0.07 \pm 0.01	Esser et al. [2004]
mc201	-77.563	166.220	256.8	-79.6	6	385.7	3.4	64.1	36.5	N	0.09 \pm 0.01	Esser et al. [2004]
mc202	-77.657	166.364	341.0	-47.1	5	3519.1	1.3	39.9	144.4	N	0.54 \pm 0.01	Esser et al. [2004]
mc203	-77.581	166.251	137.0	77.1	5	1785.1	1.8	-72.4	276.0	R		
mc204	-77.640	166.408	99.4	-75.8	5	586.7	3.2	58.8	287.0	N	0.04 \pm 0.01	Esser et al. [2004]
mc205	-77.657	166.725	284.7	-34.6	9	1716.6	1.3	21.7	86.9	N	0.37 \pm 0.02	Esser et al. [2004]
mc206	-77.667	166.780	327.6	-32.0	10	217.6	3.3	27.6	131.5	N		
mc207	-77.679	166.517	46.8	-70.6	5	313.2	4.3	62.0	229.9	N		
mc208	-77.668	166.532	38.1	-66.6	6	315.1	3.9	58.1	216.3	N		
mc209	-77.685	166.368	60.3	-61.6	6	979.8	2.2	47.8	238.1	N		
mc210	-77.691	166.374	50.0	-69.5	5	1627.2	1.9	59.8	232.3	N		
mc211	-77.661	166.340	5.0	-56.0	7	604.2	2.5	48.8	172.4	N		
mc212	-77.565	166.359	43.6	19.2	5	1207.4	2.2	-0.8	209.2	R	2.6 \pm 0.3	Fleck et al. [1972]
mc213	-77.223	166.429	180.6	70.7	5	323.6	4.3	-67.8	347.3	R		
mc214	-77.224	166.429	177.5	77.4	10	2549.0	1.0	-78.7	341.2	R		
mc215	-77.477	166.895	342.0	-79.0	10	592.1	2.0	79.9	127.1	N	0.34 \pm 0.02	Esser et al. [2004]
mc216	-77.424	166.811	346.4	-45.3	7	141.0	5.1	39.0	151.1	N	0.51 \pm 0.02	Esser et al. [2004]
mc217	-77.509	167.441	285.0	-71.5	9	129.7	4.5	57.4	73.3	N	0.16 \pm 0.01	Esser et al. [2004]
mc218	-77.562	166.978	348.6	-82.0	7	108.2	5.8	85.7	121.0	N	0.03 \pm 0.01	Esser et al. [2004]
mc219	-77.848	166.675	226.9	75.2	9	862.2	1.8	-68.7	56.4	R		
mc220	-77.457	166.910	21.9	-82.9	10	516.1	2.1	84.8	251.7	N	0.53 \pm 0.04	Esser et al. [2004]
mc221	-77.516	166.798	275.7	-82.8	6	470.3	3.2	72.2	39.5	N	0.12 \pm 0.01	Esser et al. [2004]
mc222	-77.539	166.848	190.4	-52.7	6	273.9	4.1	21.0	356.2	N	0.11 \pm 0.01	Esser et al. [2004]
mc223	-77.658	166.786	73.2	-85.6	10	327.9	2.7	77.1	305.9	N	0.38 \pm 0.03	Esser et al. [2004]
mc224	-77.530	166.884	190.2	-61.6	5	927.2	2.5	30.5	355.6	N	0.03 \pm 0.01	Esser et al. [2004]
mc225	-77.581	166.802	114.3	-74.6	9	952.3	1.7	54.4	297.8	N	0.06 \pm 0.01	Esser et al. [2004]
mc226	-77.614	166.766	17.9	-51.8	5	2216.5	1.6	44.1	187.9	N	0.24 \pm 0.02	Esser et al. [2004]
mc227	-77.271	166.733	220.3	60.3	5	2807.9	1.4	-50.3	36.3	R	4.5 \pm 0.6	Armstrong [1978]
mc228	-77.267	166.377	217.5	63.9	10	276.7	2.9	-55.0	34.3	R		
mc229	-77.483	167.154	100.0	73.0	8	346.4	3.0	-58.5	246.5	R	1.07 \pm 0.18	Esser et al. [2004]
mc01	-77.85	166.64	258.6	78.6	7	215.9	4.2	-67.3	95.2	R	1.18 \pm 0.01	Tauxe et al. [2004]
mc02	-77.85	166.69	328.6	-80.0	6	1079.2	2.1	79.0	101.2	N	0.33 \pm 0.02	Tauxe et al. [2004]
mc03	-77.84	166.76	352.0	-82.7	6	864.7	2.3	87.1	123.1	N	0.35 \pm 0.01	Tauxe et al. [2004]
mc04	-77.84	166.7	352.1	-86.8	5	292.3	4.6	84.1	355.2	N	0.34 \pm 0.01	Tauxe et al. [2004]
mc06	-77.83	166.67	13.6	-78.8	5	254.4	4.8	79.8	196.0	N		
mc07	-77.8	166.72	156.9	-69.1	5	555.9	3.2	41.2	328.3	N		
mc08	-77.8	166.83	38.5	-78.3	8	429.5	2.7	75.1	234.6	N	0.65 \pm 0.05	Tauxe et al. [2004]
mc09	-77.55	166.2	259.9	-82.7	8	234.2	3.6	69.5	30.4	N	0.07 \pm 0.02	Tauxe et al. [2004]
mc10	-77.57	166.23	335.3	-78.6	8	184.5	4.1	78.2	116.5	N		
mc11	-77.57	166.23	327.1	-77.1	8	621.8	2.2	74.4	109.0	N		
mc13	-77.64	166.41	110.5	-70.6	8	259.5	3.5	49.1	291.0	N	0.06 \pm 0.01	Tauxe et al. [2004]
mc14	-77.46	169.23	0.9	-80.8	8	439.5	2.6	84.6	172.2	N		
mc15	-77.47	169.23	166.3	84.2	9	819.9	1.8	-87.0	232.5	R	1.33 \pm 0.02	Tauxe et al. [2004]
mc19	-77.86	165.23	146.8	-78.4	7	474.8	2.8	56.9	322.9	N		
mc20	-77.88	165.02	138.7	-77.3	7	243.7	3.9	55.7	316.2	N	0.77 \pm 0.032	Tauxe et al. [2004]
mc21	-78.21	166.49	329.7	79.3	8	309.1	3.2	-58.6	146.5	R		
mc26	-78.21	166.57	13.4	-55.8	8	217.7	3.8	47.7	182.7	N		
mc28	-78.29	164.73	80.4	-84.1	7	82.1	6.7	75.0	294.4	N	0.06 \pm 0.01	Tauxe et al. [2004]
mc29	-78.31	164.8	6.9	-78.3	8	273.5	3.4	79.0	178.8	N	0.18 \pm 0.08	Tauxe et al. [2004]
mc30	-78.34	164.87	242.7	68.3	8	141.2	4.7	-55.5	62.5	R		
mc31	-78.34	164.28	298.7	-86.1	5	586.8	3.2	79.6	25.2	N		
mc32	-78.36	164.3	265.0	-74.6	7	346.5	3.2	58.1	49.9	N		
mc33	-78.38	164.34	9.6	-75.7	8	349.4	3.0	74.3	180.6	N		

Table 1. (continued)

Site	Site Latitude (°N)	Site Longitude (°E)	Dec	Inc	N	<i>k</i>	α_{95}	VGP Lat	VGP Lon	Pol	Preferred Age (Ma $\pm 2\sigma$)	Age Reference
mc34	-78.39	164.27	279.0	-81.4	7	309.9	3.4	71.2	46.9	N		
mc35	-78.39	164.23	293.6	-84.0	8	273.0	3.4	77.2	42.6	N	0.12 \pm 0.02	<i>Tauxe et al.</i> [2004]
mc36	-78.39	164.27	349.1	-83.0	7	149.2	5.0	86.8	111.2	N	0.12 \pm 0.02	<i>Tauxe et al.</i> [2004]
mc37	-78.4	164.27	210.6	82.2	8	300.6	3.2	-82.1	62.2	R	4.47 \pm 0.04	<i>Tauxe et al.</i> [2004]
mc38	-78.4	164.21	296.5	-78.0	7	258.4	3.8	69.5	71.9	N		
mc39	-78.39	164.21	263.1	-85.9	8	188.0	4.1	75.1	17.3	N	0.08 \pm 0.01	<i>Tauxe et al.</i> [2004]
mc40	-78.39	164.2	192.7	-83.1	7	140.5	5.1	64.9	351.2	N		
mc41	-78.39	164.12	270.9	-78.1	6	114.5	6.3	64.7	49.3	N	0.28 \pm 0.02	<i>Tauxe et al.</i> [2004]
mc43	-78.37	164.24	291.8	-87.8	6	177.1	5.1	79.2	6.6	N		
mc44	-78.36	164.26	324.2	-73.9	8	153.2	4.5	68.4	111.5	N		
mc48	-78.24	163.36	77.0	-56.6	7	165.4	4.8	38.9	249.5	N		
mc49	-78.24	163.36	157.0	75.0	6	140.2	5.7	-72.1	306.5	R	1.14 \pm 0.02	<i>Tauxe et al.</i> [2004]
mc50	-78.25	163.22	191.3	71.4	8	458.9	2.6	-67.5	359.8	R	1.9 \pm 0.1	<i>Tauxe et al.</i> [2004]

^aDec and Inc are mean site declination and inclination, respectively. N is the combined number of best-fit lines and planes of all the specimens used in statistical calculations, *k* is an estimate of the Fisher [1953] precision parameter, and α_{95} is the Fisher [1953] circle of 95% confidence. VGP Lat and Lon are the virtual geomagnetic poles calculated for each site. Pol. is the designated polarity determined by VGP latitude less than (reverse, R) or greater than zero (normal, N). Preferred age is the ⁴⁰Ar/³⁹Ar radiometric plateau age in Ma with 2 σ error.

3.3. Paleointensity

[23] Our study applies the IZZI variant of the Thellier-Thellier paleointensity experiment [Thellier and Thellier, 1959] to estimate intensity for 319 specimens. Selkin et al. [2007] has shown that naturally occurring assemblages of magnetic minerals can have significantly nonlinear TRM acquisition behavior. Therefore we also tested representative specimens for nonlinear magnetic field acquisition by heating, cooling, and measuring samples NRM

after exposure to increasing fields from 10 to 70 μ T. In addition, anisotropy of remanence was tested on representative specimens using anisotropy of anhysteretic remanence as a proxy for TRM anisotropy.

[24] All paleointensity experiments were performed in the paleomagnetic laboratory at Scripps Institution of Oceanography in custom-built ovens (as described above). In this experiment, the specimens were heated to a given temperature step and allowed to cool in a zero field (the zero-field step).

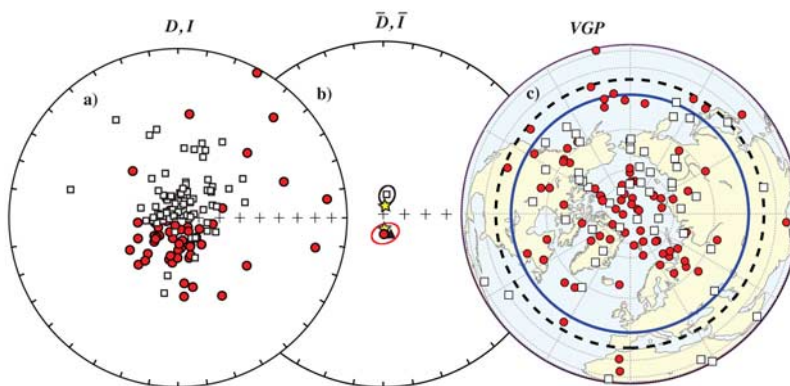


Figure 8. (a) All sites with interpretable directions where normal (white squares) and reverse (red circles) directions are defined by positive and negative Virtual Geomagnetic Pole (VGP) latitude, respectively. (b) Mean normal (white square) and reverse (red circle) direction with Fisher 95% confidence cones for sites with $n \geq 5$ and $k > 50$. The yellow stars are the directions as predicted from GAD. The black triangle is the field direction today at McMurdo Station ($D = 147^\circ$; $I = -81^\circ$). Please note that the red circle is down, while the black triangle is up. (c) VGP positions for sites with age < 5 Ma, $n \geq 5$ and $k > 50$ with the dashed circle at 36° representing the VGP latitude (λ_{VGP}) cutoff calculated using the Vandamme [1994] criteria (see text) and the solid blue line is the $\lambda_{VGP} = 45^\circ$.

Table 2. Mean Directions^a

	N	\bar{D} (°)	\bar{I} (°)
Mean	125	357.8	-81.4
Normal	76	10.7	-80.9
Reverse	49	155.6	81.3

^a N is the number sites with ages less than 5 Ma, \bar{D} is the mean declination, \bar{I} is the mean inclination, and normal and reverse are defined by positive and negative VGP latitude, respectively.

Next, the specimens were heated to the same temperature and cooled in a field applied along the specimen's cylindrical axis (in-field step). The "zero-field/in-field" method (ZI) of progressively replacing NRM with pTRM allows calculation of the NRM remaining and the pTRM gained after each temperature step through vector subtraction [after *Coe et al.*, 1978]. The IZZI method alternates the order of zero-field and in-field measurements (IZ versus ZI) at each temperature step in order to monitor inequalities in blocking and unblocking temperature (the temperature below which material can retain a remanent magnetization despite changes in applied field). This adaptation makes the IZZI method uniquely devised to monitor multidomain behavior, a non-uniform magnetization state within the rock [see *Yu et al.*, 2004], and replaces the need for the more time consuming pTRM-tail checks [Riisager and Riisager, 2001].

[25] Each paleointensity experiment consisted of a series of at least 11 IZ or ZI heating steps in a field of either 25 μT (2003/2004 field season) or 30 μT (2006/2007). After processing the data from the 2003/2004 field season, it was apparent that the sites have an average closer to 30 μT than 25 μT , and therefore the lab applied field was changed accordingly. The pTRM checks were performed every other heating step, yielding a minimum of five checks per specimen. The samples were heated until at least 95% of the NRM was demagnetized.

[26] We perform initial quality control by visually inspecting both the Arai and vector-endpoint diagrams, disregarding data for which no component is obviously linear. The remaining specimens that have relatively linear components of magnetization are interpreted for paleointensity using the following rules in order of priority: (1) The component must be linear for a minimum of four temperature steps. (2) No data are used at temperature steps higher than a failed pTRM check. (3) The temperature range of the interpreted component must be related to the characteristic remanent magnetization (ChRM) of the specimen. (4) Temperature steps are not interpreted beyond a temperature step

where the pTRM gained is lower than at a previous lower temperature step, as this is an indication of alteration.

[27] With the initial quality control complete, we further refine the interpretation of these data with the following guidelines to ensure that the fundamental assumptions of the paleointensity experiment are not violated. We use the following statistics to evaluate data quality (for further details, see *Ben-Yosef et al.* [2008] and *Tauxe and Staudigel* [2004]):

[28] The variable β , the scatter statistic, is the standard error of the slope, divided by the absolute value of the best fit slope [*Coe et al.*, 1978]. This accounts for uncertainty in pTRM and NRM data.

[29] DANG, the "deviation of the angle" is the angle between the interpreted component and the origin, as measured from the vector-endpoint diagram [*Pick and Tauxe*, 1993].

[30] MAD, the "maximum angle of deviation," is the angular uncertainty of the best fit line or plane [*Kirschvink*, 1980].

[31] The variable f_{vds} is the ratio between the y intercept of the interpreted component on the Arai plot and the total NRM of the experiment [*Tauxe and Staudigel*, 2004].

[32] DRATS, the "difference ratio sum," is the sum of differences between the original pTRM and the pTRM checks at each given temperature

Table 3. Results of Summary Statistics^a

	0–5 Ma	Brunhes	Matuyama
	<i>No Cutoff</i>		
N	125	34	41
$\overline{\Delta I}$ (°)	2.6 _{-0.6} ^{5.0}	-1.2 _{-5.8} ^{4.2}	5.4 _{1.1} ^{9.8}
S_B (°)	34.4 _{30.2} ^{38.6}	32.2 _{25.2} ^{38.7}	34.7 _{26.7} ^{42.0}
	<i>Vandamme Cutoff</i>		
N	112	31	35
$\overline{\Delta I}$ (°)	3.7 _{1.6} ^{5.7}	0.9 _{-3.0} ^{5.9}	4.6 _{1.5} ^{7.4}
S_B (°)	266 _{24.0} ^{29.2}	26.7 _{20.4} ^{31.9}	23.7 _{20.2} ^{27.2}
	$ \lambda_{\text{VGP}} < 45^\circ$		
N	104	27	35
$\overline{\Delta I}$ (°)	2.6 _{0.7} ^{4.1}	-3.1 _{-5.1} ^{-1.0}	3.8 _{1.1} ^{6.2}
S_B (°)	23.9 _{21.8} ^{26.0}	21.1 _{16.6} ^{25.1}	23.7 _{20.1} ^{26.8}

^a $\overline{\Delta I}$ is average inclination anomaly, S_B is angular dispersion. Both statistics are presented in degrees. $|\lambda_{\text{VGP}}| < 45^\circ$ indicates statistic was calculated with sites having an absolute VGP latitude greater than 45° . "Vandamme Cutoff" indicates statistic was calculated using only sites with that passed the *Vandamme* [1994] criterion (see text).

Table 4. Specimen Level Cutoff Criteria^a

Statistic	Cutoff
f_{vds}	>0.3
MAD	<11.0°
β	<0.14
DANG	<13.0
Z	<3.0
DRATS	<17.0

^a Abbreviations are given in the text.

step normalized by the pTRM of the maximum temperature step in the interpreted component [Tauxe and Staudigel, 2004].

[33] Z is a statistic that assesses the “zigzag” behavior seen in some IZZI experiments by testing for common mean slopes or directions (using the *F* test [see Ben-Yosef et al., 2008]) between the IZ and ZI steps of the interpreted component on the Arai plot or vector-endpoint diagram, respectively.

[34] The cutoff values for each specimen-level criterion used for subsequent analysis as described above are defined in Table 4. There is no single agreed upon set of criteria that define a high-quality Thellier-Thellier experiment because every data set has different mineralogy, degrees of magnetic contamination, and experimental methodologies. The list of criteria described in Table 4 was chosen to maximize the number of sites having repeatable measurements. Note, the evaluation of Tauxe et al. [2004a] used different criteria from those presented here, but the conclusions were quite similar. By including the raw data from Tauxe et al. [2004a] in this study, we (re)evaluate all specimen and site-level paleointensity analyses with consistent criteria for all Antarctica paleointensity results. A table summarizing the results and a variety of quality criteria for each interpreted specimen can be found in the supplemental material. Sixty seven percent (or 215) of the 319 specimens interpreted after visual inspection passed the specimen-level criteria described in Table 4. Many of the 215 specimens are well behaved, with statistics far better than the cutoff levels, examples of which are shown in Figure 6.

[35] As seen in the work of Ben-Yosef et al. [2008] the most dramatic improvement in consistency of paleointensity results for each site occurs as a result of setting an appropriate cutoff for DRATS, the alteration check statistic. Consequently, the cutoff value for DRATS (DRATS < 17.0) rejects more specimen intensities than other specimen-level cri-

terion choice (e.g., $Z < 3$, or $DANG < 13$). For thoroughness, we present several examples of problematic and borderline data in Figure 9 to demonstrate how the criteria selectively retain or reject particular behaviors that plague paleointensity studies and have characteristic signatures in Arai plot and vector-endpoint diagrams. For example, the specimen mc113a2 (Figure 9a) is rejected because of high DRATS (17.3), while mc113j1 is included with a slightly lower DRATS (13.2). Clearly, the pTRM checks are better for specimen mc113j1 than for mc113a2. Specimen mc225b1 is included but exhibits moderate DANG (5.7) and high MAD (7.1). Specimen mc129b1 is an example where only the low-temperature portion of the Arai plot could be interpreted because of failure of pTRM checks at high temperature steps. Yet, we do not include this specimen (or any like it) because it does not produce a component clearly associated with a ChRM, failing the third rule of our initial checks.

[36] A possible bias in paleointensity experiments is from anisotropy of remanence. Anisotropy of TRM can be detected by comparing the direction of the pTRM acquired during the Thellier-Thellier experiment with the laboratory field direction. On the basis of this comparison, a total of 20 specimens from five sites were also subjected to a nine-position anisotropy of anyhysteretic remanence (AARM). Their intensities were corrected for AARM anisotropy using the method described by Selkin et al. [2000]. In no case did the correction exceed 2 μ T.

[37] In addition to the specimen-level statistics, we evaluate site-level statistics (Table 5) to ensure that outliers do not adversely effect our final paleointensity estimation. The most fundamental site-level statistic is the number of specimens evaluated per site, N_B . We require within-site reproducibility, which means $N_B \geq 2$. There is a tradeoff between increasing the N_B cutoff and decreased number of sites available for analysis. The second site-level statistic is the standard deviation of the specimen intensities as a percent fraction of the mean intensity, which we define as $d\sigma_B = 100 \times \sigma_B/\bar{B}$. By implementing a $d\sigma_B$ cutoff, we institute further tradeoff between site reproducibility and site quantity. We explore a range of values for both of these statistics to determine the optimal pair of statistic cutoffs as well as the stability of the resultant intensity for all sites (Table 6). The resultant mean paleointensities are statistically indistinguishable for all pairs of cutoff criteria. Therefore, we choose

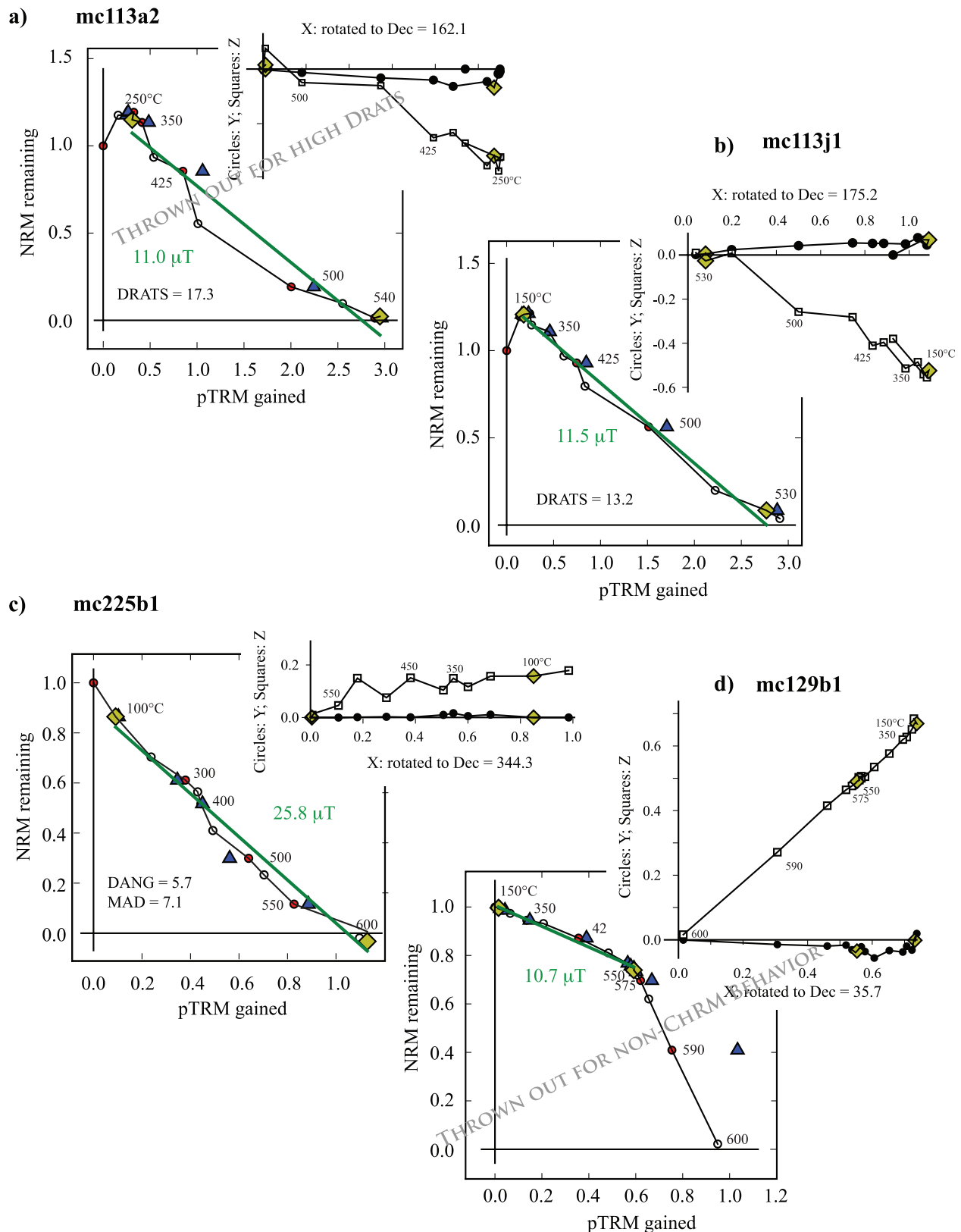


Figure 9. Same as Figure 6 for specimens (a) mc113a2, (b) mc113j1, (c) mc225b1, and (d) mc129b1 where NRM has been normalized to $3.99 \times 10^{-5} \text{ Am}^2$, $2.47 \times 10^{-5} \text{ Am}^2$, $3.71 \times 10^{-6} \text{ Am}^2$, and $3.96 \times 10^{-5} \text{ Am}^2$, respectively. These specimens represent examples of marginally acceptable paleointensity results. The specimen-level criterion(a) that a sample fails or passes are labeled in each subplot.

Table 5. Site Paleointensity Summary^a

Site	N_B	B (μT)	σ_B	$d\sigma_B$	VADM ($\times 10^{22}$ Am ²)	σ_{VADM}
mc105	4	28.6	1.9	6.7	3.8	0.3
mc109	3	34.8	1.2	3.3	4.6	0.2
mc111	2	27.9	0.4	1.5	3.7	0.1
mc113	2	11.8	0.5	3.9	1.6	0.1
mc115	2	24.6	0.4	1.8	3.2	0.1
mc116	2	39.8	1.8	4.4	5.2	0.2
mc117	4	26.4	0.7	2.8	3.5	0.1
mc119	5	41.0	2.0	4.8	5.4	0.3
mc120	5	24.3	0.7	3.0	3.2	0.1
mc123	4	30.0	2.3	7.5	3.9	0.3
mc127	2	38.5	1.5	4.0	5.0	0.2
mc128	3	34.3	2.7	7.8	4.5	0.4
mc131	5	16.8	0.9	5.3	2.2	0.1
mc132	7	3.3	0.1	4.4	0.4	0.0
mc133	2	46.3	3.5	7.5	6.1	0.5
mc140	3	17.6	3.3	18.9	2.3	0.4
mc142	3	15.6	2.7	17.5	2.1	0.4
mc145	4	6.9	0.2	3.1	0.9	0.0
mc146	2	17.2	0.7	4.1	2.3	0.1
mc147	4	22.8	2.5	11.1	3.0	0.3
mc148	3	51.6	1.6	3.0	6.8	0.2
mc154	2	8.0	1.0	12.0	1.0	0.1
mc155	3	28.9	4.6	15.9	3.8	0.6
mc160	2	21.8	1.3	5.9	2.9	0.2
mc161	2	5.0	1.2	24.3	0.7	0.2
mc164	3	81.3	0.1	0.1	10.7	0.0
mc165	4	26.3	1.7	6.4	3.5	0.2
mc167	3	43.5	1.1	2.6	5.7	0.1
mc200	3	14.3	1.2	8.6	1.9	0.2
mc214	5	43.8	3.1	7.1	5.8	0.4
mc217	5	30.3	4.6	15.2	4.0	0.6
mc218	5	34.3	2.5	7.2	4.5	0.3
mc219	4	30.3	3.8	12.6	4.0	0.5
mc220	4	53.9	1.2	2.3	7.1	0.2
mc223	4	21.5	2.7	12.3	2.8	0.3
mc225	4	28.6	3.1	11.0	3.8	0.4
mc229	3	31.2	3.9	12.6	4.1	0.5
mc01	4	16.5	3.4	20.4	2.2	0.4
mc08	3	43.4	1.5	3.5	5.7	0.2
mc09	3	27.1	1.0	3.7	3.6	0.1
mc13	3	30.4	2.2	7.2	4.0	0.3
mc15	3	28.0	2.6	9.2	3.7	0.3
mc21	4	45.0	3.4	7.6	5.9	0.4
mc30	4	42.6	0.4	0.9	5.6	0.1
mc35	2	24.1	2.8	11.5	3.2	0.4
mc36	4	25.7	3.0	11.5	3.4	0.4
mc37	4	60.4	5.3	8.7	7.9	0.7

^a N_B is the number of specimens meeting the minimum specimen-level criteria and used to calculate site mean intensity. B (μT) is the average field strength per site, σ_B is standard deviation of the specimens used to calculate the site average intensity (B), and $d\sigma_B$ is the standard deviation of the specimen intensities as a percent fraction of the mean intensity. VADM is the virtual axial dipole moment and σ_{VADM} is the standard deviation of the specimens used to calculate the average VADM.

Table 6. Average Paleointensity Results^a

Criteria	Age	N_{sites}	\bar{B} (μT)	STD Error
$N_B \geq 2, d\sigma_B \leq 20$	no cutoff	45	30.8	2.2
$N_B \geq 3, d\sigma_B \leq 20$	no cutoff	35	32.1	2.6
$N_B \geq 2, d\sigma_B \leq 15$	no cutoff	41	31.5	2.4
$N_B \geq 3, d\sigma_B \leq 15$	no cutoff	31	33.3	2.8
$N_B \geq 2, d\sigma_B \leq 10$	no cutoff	33	33.3	2.8
$N_B \geq 3, d\sigma_B \leq 10$	no cutoff	25	34.9	3.4
All specimens	no cutoff	319	29.6	1.1
$N_B \geq 2, d\sigma_B \leq 15$	0–5 Ma	32	30.8	2.7
$N_B \geq 2, d\sigma_B \leq 15$	0–0.78 Ma	12	32.1	3.4
$N_B \geq 2, d\sigma_B \leq 15$	0.78–2.58 Ma	18	29.9	3.7

^aCriteria define the set of site-level cutoffs used to determine an acceptable site result. Age is the range of ages used to calculate the average location paleointensity \bar{B} . N_{sites} is the number of sites used to calculate \bar{B} . STD error is the standard deviation of the mean paleointensity.

$N_B \geq 2$ and $d\sigma_B \leq 15.0$ to maximize the number of sites (and ages) interpreted in this study, providing a mean paleointensity of 31.5 ± 2.4 μT . The equivalent virtual axial dipole moment (VADM) is $4.1 \pm 0.3 \times 10^{22}$ Am².

[38] In order to assess the effect of differing data interpretation and selection schemes, we thoroughly explored data quality control parameters for the Antarctica paleointensity database, (re)interpreting the Arai plots multiple times. For example, following *Macouin et al.* [2006], we tried picking only specimens exhibiting a single component of magnetization (no kink or sag) and having an f_{vds} quality parameter (the fraction of the NRM component used in the slope estimation) >0.7 . This results in 21 sites having paleointensity estimates that meet the standard deviation criterion; these average to 31.9 ± 3.6 , which is statistically indistinguishable from the values in Table 6. Interestingly, even if no specimen- or site-level criteria are used, the average intensity (29.6 ± 1.1 μT) for all 319 interpreted specimens (specimen Thellier-Thellier results are in Table S1 in the auxiliary material and in the MagIC database).¹ Given the variety of data quality criteria we tested, we are confident that the mean paleointensity and corresponding standard deviation are robustly determined.

4. ⁴⁰Ar/³⁹Ar Methods and Results

[39] We selected 21 normal and reverse polarity sites from the 2003/2004 field season for new age determinations by the ⁴⁰Ar/³⁹Ar incremental heat-

¹Auxiliary materials are available in the HTML. doi:10.1029/2008GC002072.

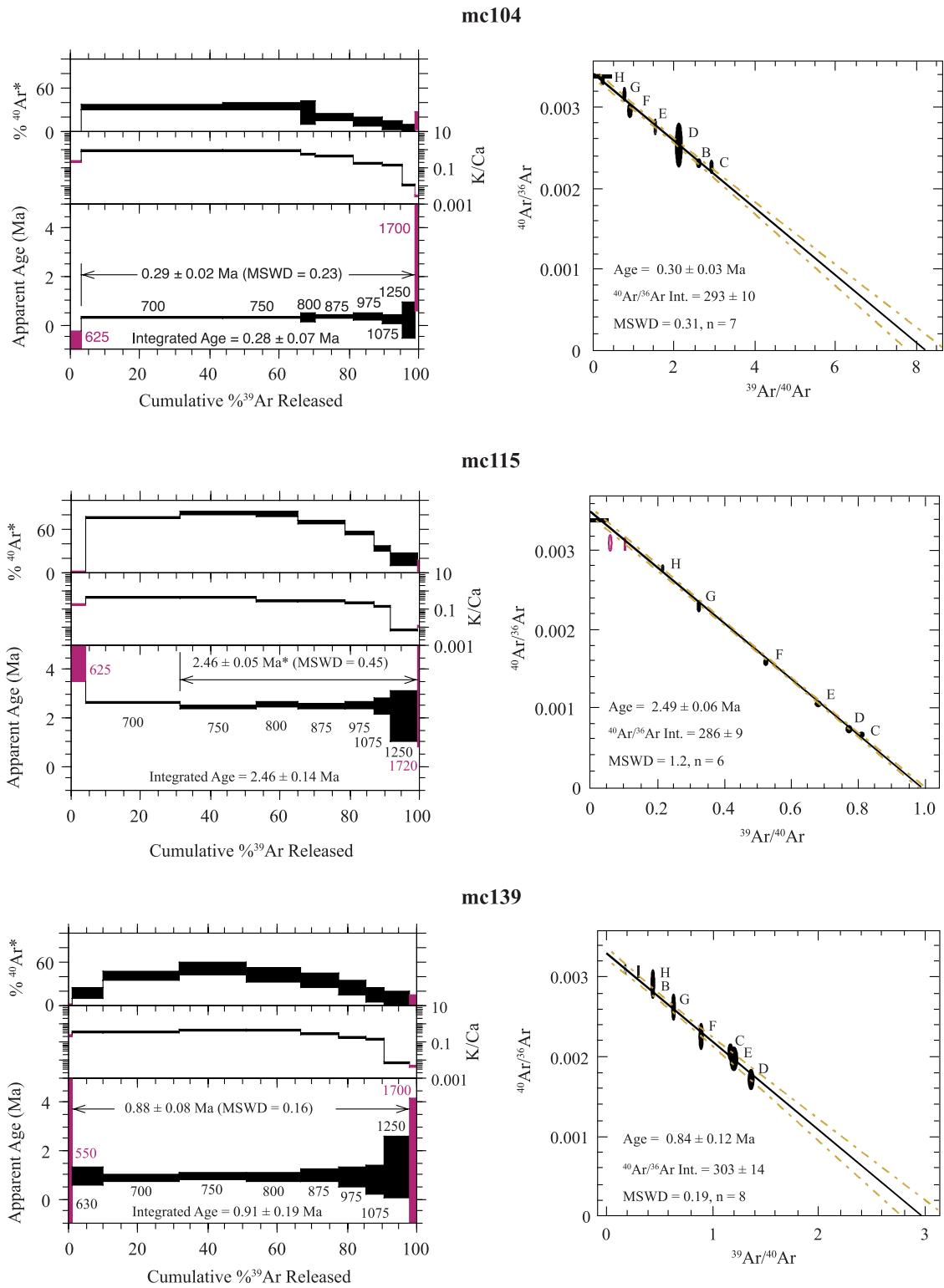


Figure 10

Table 7. Summary of $^{40}\text{Ar}/^{39}\text{Ar}$ Plateau Ages From Groundmass in 21 Lava Flows^a

Sample	Preferred Age					Isochron Age			
	Steps (°C)	% ³⁹ Ar	MSWD	K/Ca ± 2σ	Age ± 2σ, Ma	n	MSWD	⁴⁰ Ar/ ³⁶ Ar ± 2σ	Age ± 2σ, Ma
mc100	625–875	67.1	0.81	0.1 ± 0.0	0.86 ± 0.23	5	1.4	303.3 ± 8.0	0.86 ± 0.23
mc104	700–1250	95.6	0.23	0.6 ± 0.6	0.29 ± 0.02	7	0.31	292.7 ± 10.1	0.30 ± 0.03
mc106	625–1075	84.7	0.83	0.2 ± 0.0	13.42 ± 0.18	7	0.84	282.3 ± 29.7	13.53 ± 0.29
mc108	625–875	73.5	1.42	0.2 ± 0.2	0.41 ± 0.14	5	1.61	327.8 ± 67.7	0.18 ± 0.14
mc111	700–875	75.8	0.76	0.3 ± 0.2	1.99 ± 0.04	4	0.53	329.2 ± 62.82	1.90 ± 0.17
mc115	750–1250	68.1	0.45	0.3 ± 0.3	2.46 ± 0.31	6	1.24	286.0 ± 9.1	2.49 ± 0.06
mc118	625–1075	93.7	1.67	0.6 ± 0.4	0.31 ± 0.04	7	1.7	297.6 ± 11.8	0.31 ± 0.04
mc122	750–1075	68.0	1.37	0.5 ± 0.3	12.70 ± 0.09	5	1.52	272.5 ± 42.7	12.76 ± 0.13
mc123	700–1075	87.0	1.27	0.4 ± 0.3	1.93 ± 0.05	6	1.37	288.8 ± 11.9	1.97 ± 0.07
mc124	700–1250	92.0	1.79	0.3 ± 0.3	12.61 ± 0.11	7	2.28	281.8 ± 12.3	12.69 ± 0.11
mc130	700–975	58.5	0.84	0.3 ± 0.2	7.25 ± 0.07	5	0.55	251.0 ± 57.5	7.36 ± 0.15
mc134	700–975	84.5	1.48	0.3 ± 0.1	9.02 ± 0.05	5	6.09	297.3 ± 15.3	9.02 ± 0.07
mc139	625–1250	97.0	0.16	0.3 ± 0.3	0.88 ± 0.08	8	0.19	303.1 ± 13.8	0.84 ± 0.12
mc140	700–875	69.7	0.49	0.3 ± 0.1	2.03 ± 0.09	4	0.07	351.6 ± 112.9	1.80 ± 0.48
mc142	700–975	79.7	2.01	6.8 ± 3.9	1.23 ± 0.02	5	2.92	287.1 ± 138.0	1.24 ± 0.11
mc143	625–1250	75.9	1.03	0.0 ± 0.0	2.08 ± 0.65	8	1.02	302.3 ± 8.5	1.83 ± 0.68
mc164	750–1250	76.8	0.97	15.3 ± 19.2	1.36 ± 0.01	6	1.17	298.0 ± 4.5	1.36 ± 0.01
mc165	700–1250	84.8	0.68	0.4 ± 0.4	1.45 ± 0.06	7	0.73	288.6 ± 8.7	1.47 ± 0.07
mc166	625–1075	93.0	2.70	0.7 ± 0.5	1.33 ± 0.12	7	2.44	334.5 ± 42.5	1.19 ± 0.16
mc168	625–975	85.3	1.67	0.5 ± 0.3	1.38 ± 0.05	6	1.77	303.9 ± 14.0	1.34 ± 0.07
mc170	700–1075	74.1	0.79	0.3 ± 0.1	1.03 ± 0.10	6	0.99	298.2 ± 23.0	1.00 ± 0.27

^aAges are calculated relative to FC-2 Fish Canyon Tuff sanidine interlaboratory standard (28.02 Ma, [Renne *et al.*, 1998]). Analyses were performed at New Mexico Geochronology Research Laboratory using an MAP 215-50 mass spectrometer on line with automated all-metal extraction system. All errors are reported at ±2σ. MSWD is mean square weighted deviate. Details of irradiation, analytical procedures, calculation methods, and analytical data are in the auxiliary material.

ing method in the geochronology laboratory at New Mexico Tech. Fresh groundmass concentrates weighing 50–100 mg were prepared by crushing and sieving optimally chosen samples and then washing the fractions in diluted HCl. Standard magnetic separation techniques and hand-picking were employed to remove phenocryst phases including olivine, pyroxene, and calcic plagioclase. Splits from each sample were loaded into machined aluminum discs and irradiated in one batch (NM-207) for 6 h in the D-3 position at the Nuclear Science Center, College Station, Texas. They were then allowed to cool for 3 months. Samples were degassed using a double vacuum resistance furnace with molybdenum crucible and crucible liner with a heating duration of 10 min. Reactive gas species

were removed using two SAES GP-50 getters operated at ~450°C and one getter at 20°C prior to isotope separation in the Mass Analyzer Products Limited (MAP) 215–50 noble gas mass spectrometer. J factors were determined to a precision of ±0.1% by CO₂ laser-fusion of six single crystals from each of six radial positions around the irradiation tray. Correction factors for interfering nuclear reactions were determined using K-glass and CaF₂. Ages are calculated using the decay constants and isotopic abundances from Steiger and Jäger [1977] and are calculated relative to FC-2 Fish Canyon Tuff sanidine interlaboratory standard (28.02 Ma [Renne *et al.*, 1998]). Reported plateau ages for step-heated samples are weighed by the inverse variance for the steps

Figure 10. Examples of (a, c, and e) $^{40}\text{Ar}/^{39}\text{Ar}$ spectra and (b, d, and f) inverse isochrons from selected samples. $^{40}\text{Ar}/^{39}\text{Ar}$ spectra are plotted against cumulative fraction of ^{39}Ar released, including the apparent age at each temperature step (°C) (bottom), the K/Ca ratio (middle), and the radiogenic % $^{40}\text{Ar}^*$ yield from the individual heating steps. The black arrow indicated the steps used in the calculation of the weighted mean plateau age. Steps excluded from age calculation are shown in pink. The middle plots of Figures 10a, 10c, and 10e are the K/Ca ratio for each heating step. Inverse isochrones include an indication of the results for individual heating steps (A–H), a best fit line (black) and associated error (yellow dashed) calculated from regression results of York [1969]. Isochron age and initial $^{40}\text{Ar}/^{36}\text{Ar}$ values are also reported. All errors reported are 2σ with the error in J and MSWD is mean square deviate.

which met plateau criteria (three or more contiguous steps comprising more than 50% of ^{39}Ar released which agreed to within $\pm 2\sigma$). Imprecise, low-radiogenic-yield initial and final steps were excluded from age plateaus. MSWD (mean square weighted deviate) values are calculated for each weighted mean, and errors are determined using the method of Taylor [1982]. If the MSWD value is greater than 1, the error is multiplied by the square root of the MSWD. Details of the analytical methods and the analytical data are available in the EarthRef Digital Archive (ERDA) and Table S2 in the auxiliary material.

[40] All samples, with the exception of mc100 and mc143 yielded fairly flat age spectra having well-defined, relatively precise ($\pm 2\sigma < 0.2$ Ma) plateau ages that agree within error with isochron intercept ages. All isochrons have $^{40}\text{Ar}/^{36}\text{Ar}$ intercepts within error of the atmospheric value (295.5) indicating no significant excess ^{40}Ar is present in the dated groundmass concentrates. Examples of selected age spectra and correlation diagrams are shown in Figure 10. A summary of age information is provided in Table 7 which displays $^{40}\text{Ar}/^{39}\text{Ar}$ ages ranging from 0.29 ± 0.02 Ma to 13.42 ± 0.18 Ma, with all errors given as $\pm 2\sigma$.

5. Discussion

[41] The data set presented here provides a unique opportunity to examine paleointensity and paleodirection at high latitude. Although this study sampled sites with ages spanning 0 to 14 Ma, we limit our analyses to data spanning the past 5 Ma for two reasons: first, the number of data available diminishes rapidly with increasing age; second, for ages less than 5 Ma the plate motion corrections needed to obtain accurate paleosite locations are small and reasonably well known. Note, we did not perform plate rotation corrections because rotations are insignificant for the past 5 Ma at this location. Given the temporal sampling of this study, we present analyses of Brunhes-age normal polarity data, Matuyama-age reverse polarity data, and 0–5 Ma combined normal and reverse polarity data separately. In addition to presenting new 0–5 Ma directional and intensity data, we analyze all available Antarctic data with ages in the 0–5 Ma time interval. All data and subsequent interpretations presented here are available in the MagIC database at <http://earthref.org/cgi-bin/magic.cgi?mdt=m000629dt20080226180017>. The complete data set analyzed includes directional (133 sites) and intensity (47 sites) results from this new study and

results from Tauxe *et al.* [2004a] from the same volcanic province. The intensity results from the previous study were reanalyzed to maintain consistency in specimen-level quality. All sites from this combined data set have $k > 50$ and $n \geq 5$, criteria suggested by Johnson *et al.* [2008] as requirements for high-quality directional data. A total of 91 sites from the combined data set have associated radioisotopic $^{40}\text{Ar}/^{39}\text{Ar}$ dates ranging from 0.026 Ma to 13.422 Ma, of which eight sites are older than 5 Ma. This data set represents a substantial number of sites meeting our reliability criteria (Figure 8a). The directions are not Fisher distributed (the inclinations are long-tailed relative to an exponential distribution). However, the mean direction is indistinguishable from GAD (Figure 8b).

[42] The inclination anomalies, presented here, provide important high-latitude constraints on the TAF. The observation of negligible 0–5 Ma inclination anomaly ($< 3^\circ$, Table 3) at this location is not unexpected as previous observational and modeling studies predict the largest inclination anomaly at equatorial latitudes (see review in the work of Johnson and McFadden [2007]). The good temporal distribution of these high-quality data enable us to compare behavior between the Brunhes and Matuyama polarity chrons, as there are an unusually large number of samples with ages between 0.78 and 2.58 Ma; these show a small mean negative inclination anomaly during the Brunhes and a larger-amplitude positive mean inclination anomaly during the Matuyama. This is consistent with the conclusions of Johnson *et al.* [2008] that inclination anomalies are small and negative for the Brunhes, and in the southern hemisphere, are larger and positive in the Matuyama.

[43] We also investigate VGP dispersion to characterize PSV behavior. As presented by McElhinny *et al.* [1996] many studies have observed polarity chron dependence of dispersion, where the Matuyama (as compared to the Brunhes) is often associated with higher than average dispersion. For the EVP study, regardless of the VGP cutoff applied, we find no evidence for differences in dispersion for the Brunhes and Matuyama polarity chrons. Using all the data (taking the antipodes of the reverse poles), S_B is 34.4° (with bootstrap confidence bounds of 30.2° – 38.6°). Using the Vandamme [1994] colatitude cutoff of 52.9° ($|\lambda_{\text{VGP}}| < 37.1^\circ$ latitude) S_B is 26.6° [24.0° – 29.2°]. Using the $|\lambda_{\text{VGP}}| < 45^\circ$ cutoff, results in $S_B = 23.9^\circ$ [21.8 – 26.0]. Moreover, the dispersion confidence bounds for all data (0–5 Ma), the normal Brunhes, or the reverse

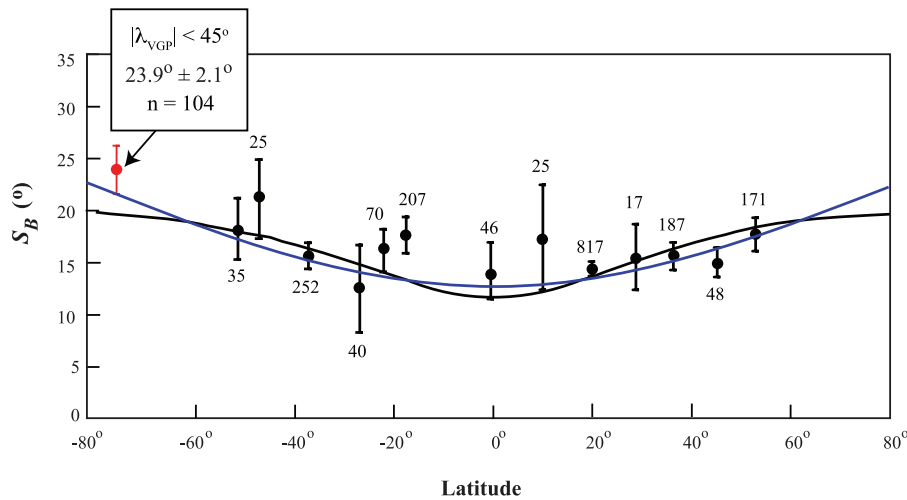


Figure 11. VGP dispersion (S_B) as a function of latitude. The mean dispersion for the Erebus Volcanic Province shown as a red circle, all other data from *Johnson et al.* [2008] shown as black circles. Errors bars are 2σ . All data have $k > 50$, age < 5 Ma, and $|\lambda_{VGP}| < 45^\circ$. Model G [*McFadden et al.*, 1988] shown in blue and model, TK03 [*Tauxe and Kent*, 2004] shown in black.

Matuyama chron overlap one another, although the reverse data seem to be slightly more scattered ($S_B = 34.7^\circ$ [26.7°–42.0°]) compared to the normal data ($S_B = 32.2^\circ$ [25.2°–38.7°]). The decreased dispersion when applying a cutoff results from the classification of either 10% or 16% of the data as transitional for the Vandamme and $|\lambda_{VGP}| < 45^\circ$ cutoffs, respectively. The mean dispersion calculated with the Vandamme λ_{VGP} cutoff is slightly higher than (but statistically indistinguishable) from that of the $|\lambda_{VGP}| < 45^\circ$ cutoff as a result of fewer low VGP latitude data being removed with the Vandamme cutoff. All estimates of dispersion are within uncertainty of the dispersion recorded in a sediment core ($30.0 \pm 4.3^\circ$) in the Ross Sea by *Jovane et al.* [2008].

[44] While not significantly dependent on polarity for this region, the dispersion results presented here do support the observation of a latitudinal variation in dispersion in the southern hemisphere. This is apparent when the Antarctic results are compared with those from other recent directional data sets [*Johnson et al.*, 2008] (Figure 11). The high dispersion is not a function of poor data quality as this data set passes all the criteria set out by *Johnson et al.* [2008]. We compare the new high-latitude dispersion results with predictions from two PSV models, Model G [*McFadden et al.*, 1988] and a more recent statistical model, TK03 [*Tauxe and Kent*, 2004]. Statistical PSV models, such as TK03, allow the prediction of geomagnetic field vectors at any location, by modeling the time-varying geomagnetic field as a “Giant Gaussian

Process” in which the spherical harmonic coefficients are assumed to be temporally independent random variables with Gaussian distributions (see *Johnson and McFadden* [2007] for a review). The high dispersion at -78° is underestimated by the PSV model TK03, but consistent with Model G. Clearly, PSV models that predict flat (e.g., CP88 [*Constable and Parker*, 1988]) dispersion with latitude do not explain the Southern Hemisphere observations.

[45] A common assumption is that the time-averaged geomagnetic field can be approximated by a dipole. The intensity of an axial-dipole field varies with latitude according to the following equation:

$$B = g_1^0 (1 + 3 \cos^2 \theta)^{1/2}, \quad (4)$$

where g_1^0 is the axial dipole term in the spherical harmonic expansion and θ is colatitude. Consequently, the intensity at either pole should be twice that of the equatorial value. Today’s field (represented by IGRF2005) has a latitudinal dependence (blue line in Figure 12) that is strikingly similar to that of a dipole, with a g_1^0 term equal to $30 \mu\text{T}$. The statistical PSV model, TK03 shows a similar pattern of increase in intensity near the poles. However, when paleointensities from the 0–5 Ma time period are plotted versus latitude, evidence for a dominantly dipole field is not obvious. Figure 12 shows site-averaged paleointensity estimates (1158 gray crosses) derived from the Pint08 database [*Biggin et al.*, 2008]. For consistency, all data from

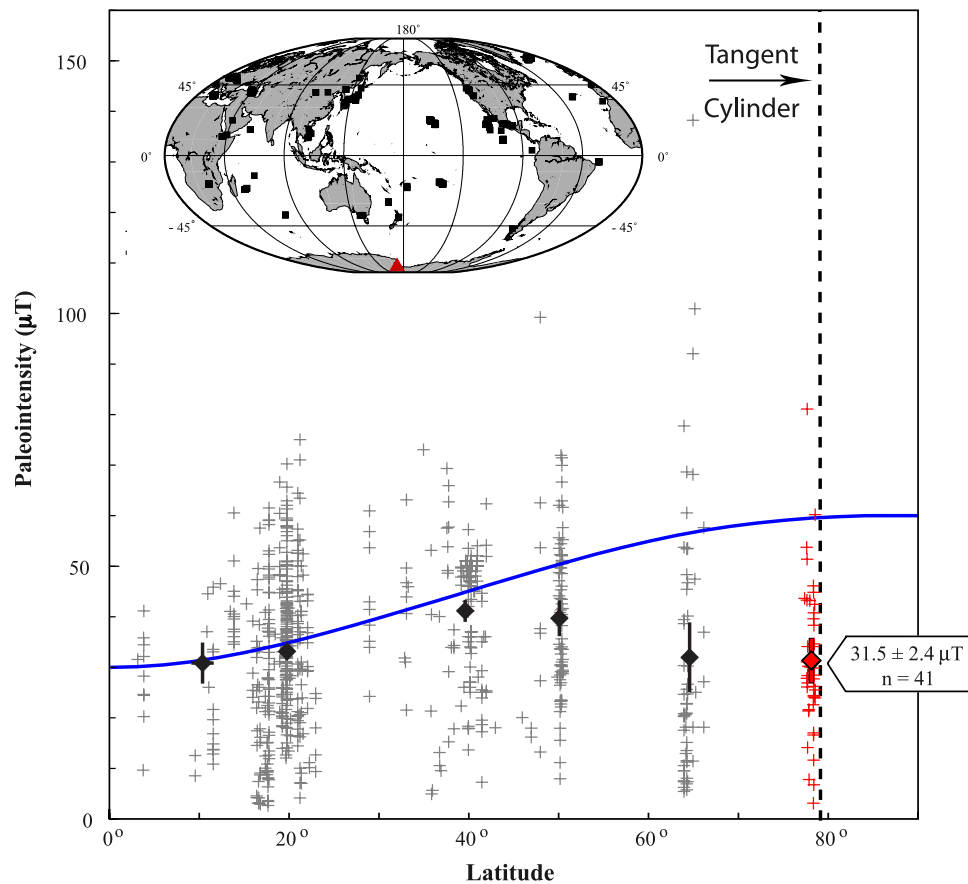


Figure 12. Paleointensity versus latitude of the Pint08 database (gray crosses) [Biggin *et al.*, 2008] and paleointensity estimates from this study (red crosses) for data with ages less than 5 Ma, $d\sigma_B \leq 15\%$, and $N_B \geq 2$. Southern Hemisphere data have been flipped to the Northern Hemisphere. Mean paleointensity results (black diamonds) are calculated for 15° latitude bins and errors are shown as 2σ . The locations of the paleointensity results are shown in the inset with the Antarctica data set as a red triangle. The vertical dashed line is the surface expression of the edge of the tangent cylinder. The blue line represents the intensity associated with a geocentric axial dipole with a dipole term of $30 \mu\text{T}$.

Pint08 included in Figure 12 pass the same site-level criteria as outlined in section 3.3. Southern Hemisphere data are combined with the Northern Hemisphere to minimize the influence of latitudinal gaps. To reduce the effects of regional variations, the site-level estimates are averaged in 15° latitude bins (black diamonds) with 95% confidence levels calculated using a bootstrap technique. For comparison, all Erebus Volcanic Province paleointensities are plotted on Figure 12 as red crosses, and the associated mean is plotted as a red diamond with corresponding 95% confidence level of the mean.

[46] The 0–5 Ma mean paleointensity for Erebus (red diamond) is well determined and is low ($31.5 \pm 2.4 \mu\text{T}$) relative to current intensity ($\sim 63 \mu\text{T}$). Outliers do not heavily bias the mean as the median lies within the 95% confidence intervals from the

mean; moreover there is only one site with an intensity greater than $63 \mu\text{T}$. The intensities for both the Brunhes ($32.1 \pm 3.4 \mu\text{T}$) and Matuyama ($29.9 \pm 3.7 \mu\text{T}$) magnetic chrons are low and statistically indistinguishable from each other and from the 0–5 Ma mean. The relatively high dispersion and low intensity observed here agrees with the global observation of anticorrelation between dispersion and intensity [e.g., Bogue and Coe, 1984; Love, 2000].

[47] We consider several possible hypotheses for the lack of high 0–5 Ma high-latitude intensities and specifically for those presented here. We evaluate three potential scenarios: (1) data bias resulting from poor selection criteria or laboratory bias, (2) poor temporal/spatial sampling, or (3) persistent anomalous field behavior at this location. First, we address the issue of data quality. The data quality

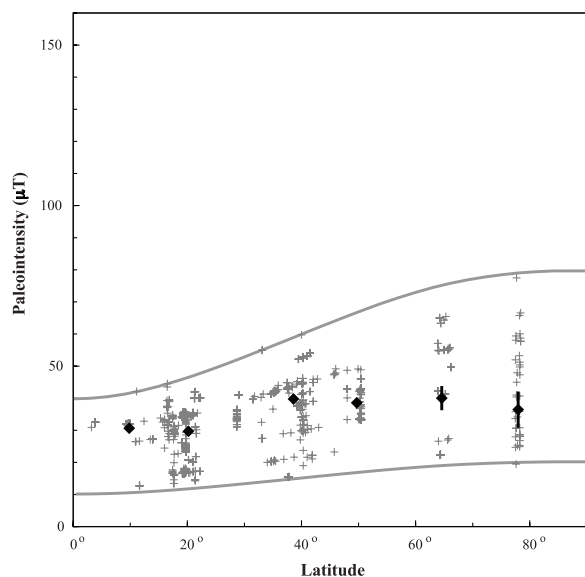


Figure 13. Paleointensity versus latitude for a theoretical dipole with time-varying intensity sampled at equivalent times and locations (grey crosses) as the Pint08 and Antarctica databases. Mean paleointensity (black diamonds) was calculated for every 15° latitude bin. For reference, grey lines are dipole fields with mean values of 10 (lower) and 40 (upper) μT .

control parameters for the Antarctica paleointensity data set were extensively tested. We applied our own set of quality criteria described above but also tested other selection criteria [e.g., *Macouin et al.*, 2006; *Tauxe et al.*, 2004a]. We also assessed the possibility of inaccurate (nonlinear) TRM acquisition, bias from anisotropy of TRM, or inappropriate (multidomain) magnetic carriers within the field specimens with positive results. From our investigations we conclude that the low average intensity for the EVP is a robust result.

[48] Next, we investigate possible bias introduced by uneven temporal sampling given that field intensity varies over long timescales. We model the ancient field as a dipole using a time-varying intensity, $g_1^0(t)$, with a functional power spectrum, $g_1^0(f) = \frac{1}{1+c \cdot f^2}$, where c is a constant [*Ziegler et al.*, 2008]. The functional form approximates the power spectrum of the 0–160 Ma paleointensity data set [*Constable and Johnson*, 2005] and has constant power to a corner frequency of 10^{-5} a^{-1} and power law decay thereafter.

[49] We generate 100 time-varying models from random time series that have the above-mentioned functional power spectrum. The minimum and maximum allowable values of the g_0^1 term are set to 5 and 60 μT for each random time series. Then

we sample the hypothetical field intensities at site locations and associated ages equivalent to the Pint08 and EVP data sets. The theoretical time- and latitude-dependent intensity for each site is determined using equation (4) and the time-dependent $g_1^0(t)$ term generated with the functional power spectrum described above. This generates 100 new theoretical paleointensity data sets with a latitude-age distribution corresponding to the same data points within the Pint08 and EVP data sets. We then determine the average intensity for 15° bins as done above. While many of the resultant time- and latitude-dependent average intensities for the 100 hypothetical data sets increase with latitude, many do not, of which one example is shown in Figure 13. Approximately two out of three resultant intensity-latitude distributions were dampened/flattened to some degree. Nearly half of the modeled average intensity-latitude distributions had lower intensity at high latitude than midlatitude. In Figure 13 the minimum and maximum values of the g_1^0 term were 10 and 40 μT , providing a relatively flat intensity-latitude distribution. We do not attempt to optimize for a preferred model because there are an infinite number of possible theoretical solutions that could use random, sinusoidal, cosinusoidal, Gaussian, or uniform time varying functions for the g_1^0 term in the 0–5 Ma period. Instead we have merely demonstrated that a flat intensity with respect to latitude may result from nonuniform temporal sampling of a time varying field. As with the 0–1 Ma time interval [*Ziegler et al.*, 2008], the current 0–5 Ma data compilation appears to still have insufficient temporal sampling to robustly characterize the 0–5 Ma dipolar intensity.

[50] Next, we test whether spatial bias due to nonuniform sampling of the global magnetic field can produce similarly flat intensity with respect to latitude. We simulate paleointensities using the PSV model TK03 at the same locations as Pint08 and our Antarctica sites. We simulate 100 points per site and find little effect due to spatial biasing. When the results are averaged in 15° bins, the averages show an increase in intensity with latitude. The results from this and the previous tests indicate that inadequate spatial sampling is less significant than inadequate temporal sampling in the paleointensity database.

[51] Temporal bias can neither be verified nor ruled out by the above test; hence we explore the likelihood of a persistent low field intensity. Strikingly, only two high-quality sites have intensities greater than 60 μT (the approximate present-day

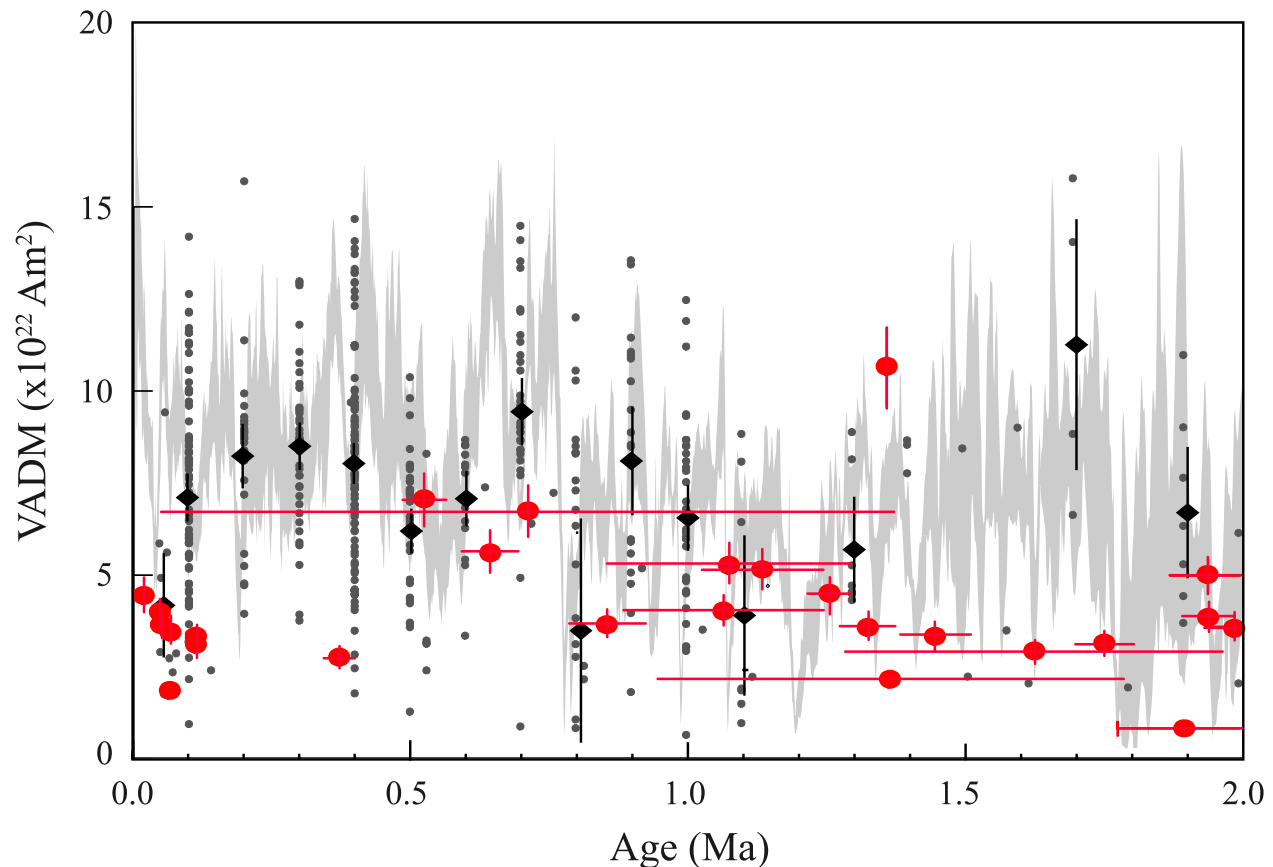


Figure 14. VADM (virtual axial dipole moment) versus time for the past 2 Ma. Site-level averages and associated standard error for both VADM and age of the Antarctica data are shown as red circles with error bars. Site-level averages of the global paleointensity database, Pint08 [Biggin *et al.*, 2008] are shown as black circles and pass the same site-level quality criteria as the Antarctica data ($N_B \geq 2$, $d\sigma_B < 15\%$). Error for these measurements has been omitted for clarity. The global data set was then binned in 200,000 year time intervals and averaged (black diamonds with standard error shown). Finally the 95% confidence bounds of Sint2000 [Valet *et al.*, 2005] are shown in gray.

field intensity at McMurdo). We investigate the persistence of the EVP intensity low by comparing estimates of the EVP virtual axial dipole moments (VADM, a latitude-independent intensity) with global VADM values from data sets Pint08 [Biggin *et al.*, 2008] and Sint2000 [Valet *et al.*, 2005] over time. Figure 14 plots VADM over time for the past 2 Ma. All volcanic VADM estimates, both EVP and PINT08, pass the site-level quality criteria presented above ($N_B \geq 2$, $d\sigma_B < 15\%$). Figure 14 is limited to 2 Ma owing to the paucity of older data.

[52] The 200 ka Pint08 averages (black diamonds) and Sint2000 95% confidence intervals (gray bar) are higher than EVP (red circle) estimates for the majority of the past 2 Ma. Note the high density of EVP data from 1.1 to 2 Ma when the rest of the global volcanic data are rather sparse. Conversely, the Antarctica data are virtually absent between 0.2 and 0.5 Ma, while the global distribution there is

relatively dense. Although the majority of EVP VADM estimates are low compared to the global data sets, they do fall within the overall observed range of Pint08 values. The Antarctic data appear particularly low for the 0–0.5 Ma and 1.2 to 1.7 time intervals (where both EVP and Pint08 data are sparse). Temporal biasing may be a strong contributing factor, but it is difficult to explain consistently low VADMs where there is seemingly good data coverage without calling upon persistent anomalous geomagnetic field behavior.

[53] The persistently anomalous field behavior may result from geodynamical differences in the outer core [e.g., Aurnou *et al.*, 2003; Gubbins *et al.*, 2006; Hulot *et al.*, 2002; Jackson *et al.*, 2000; Olson and Aurnou, 1999]. Most modern dynamo simulations reproduce first-order properties of the geomagnetic field: dipole dominance and the approximate field strength [e.g., Glatzmaier *et al.*, 1999; Sakuraba and Kono, 1999; Sreenivasan and

Jones, 2006]. Within the tangent cylinder, numerical geodynamo models [e.g., Olson and Aurnou, 1999; Sreenivasan and Jones, 2005, 2006] yield polar vortices with vigorous upwellings or downwellings associated with magnetic flux minima and maxima, respectively [e.g., Christensen *et al.*, 1998]. Convergent flow associated with downwellings entrains magnetic field lines and enhances the field intensity, whereas the divergent flow of upwellings has the opposite effect. At the CMB these effects are observed in downward continued field models (derived from real observations) in the form of intense flux lobes close to the tangent cylinder and low field strength near the poles. The flux patches are major contributors to the dipole field but the contrast with low polar flux also demonstrates the presence of nondipole components of the geomagnetic field. Variations in amplitude and or position of the flux lobes may translate into greater VGP dispersion at the Earth's surface near the boundary of the tangent cylinder. However, the reduced field strength within the tangent cylinder occurs over such a small area that it is virtually impossible to detect in surface paleomagnetic data because of poor resolution in the observed field. Upward continuation of the magnetic signal from the CMB smoothes out small-scale or low-amplitude variations in the field at the CMB; furthermore, small-scale high harmonic degree anomalies ($>l = 12$ or <3000 km) at the core are generally indistinguishable from crustal sources at the Earth's surface [Kono *et al.*, 2000]. This could easily render any small scale drifting magnetic features at the CMB undetectable at Earth's surface.

[54] Further investigations of spatiotemporal properties of geodynamo models exhibiting polar vortices may help to make realistic comparisons with paleomagnetic data and model outputs. Both the high dispersion and low intensity seen at this locale may indicate some unusual behavior at the pole due to the mode of convection in the tangent cylinder. However, we cannot differentiate among the possible causes until we have both a more uniformly sampled data set and geodynamical models that can provide paleomagnetic observables for million year timescales.

6. Conclusions

[55] The analyses of new volcanic sites in the Erebus Volcanic Province (EVP), Antarctica from two recent field seasons and previous results from Tauxe *et al.* [2004a] provide evidence for high

dispersion and low intensity at high latitude (-78°). These studies collectively provide 125 high-quality new sites with well-constrained directional data ($n \geq 5$ and $k > 50$) and ages ranging from 0 to 5 Ma. The directions have a non-Fishsonian distribution and a mean direction with a small inclination anomaly ($\sim 3^\circ$). Despite the small inclination anomaly, the mean direction is indistinguishable from GAD or the current field direction at McMurdo.

[56] New $^{40}\text{Ar}/^{39}\text{Ar}$ ages were determined for 21 new reverse and normal polarity sites yielding ages from 0.86 to 13.42 Ma. With these new radioisotopic dates and existing dates from Esser *et al.* [2004], Wilch [1991], and Wilch *et al.* [1993], 91 of the high quality sites investigated here were radioisotopically dated, so results from Brunhes and Matuyama chrons may be compared. For the Erebus volcanic province study, the dispersion for all data (0–5 Ma), the normal Brunhes, or the reverse Matuyama chron are statistically indistinguishable from each other. This holds regardless of the λ_{VGP} cutoff applied (none, Vandamme, or $|\lambda_{\text{VGP}}| < 45^\circ$), although specific value of the dispersion changes with λ_{VGP} cutoff. Yet, the dispersion for the Erebus Volcanic Province is high ($23.9 \pm 2.1^\circ$ for a cutoff of 45°) in comparison to dispersion from middle to low latitudes. This result is quite robust and is not a function of poor data quality as proposed by Johnson *et al.* [2008]. Interestingly, Model G fits the EVP dispersion within the 95% confidence intervals, while the PSV model, TK03, underestimates the measured dispersion.

[57] IZZI and Coe modified Thellier-Thellier experiments provided 41 high-quality paleointensity estimates, for which 76% have associated radioisotopic dates. The mean EVP paleointensity is $31.5 \pm 2.4 \mu\text{T}$ for 0–5 Ma and is low relative to current intensity ($\sim 63 \mu\text{T}$) at McMurdo. The intensities for both the Brunhes ($32.1 \pm 3.4 \mu\text{T}$) and Matuyama ($29.9 \pm 3.7 \mu\text{T}$) magnetic chrons are also low, and statistically indistinguishable from each other and the 0–5 Ma mean. The observed high dispersion and low intensity are predicted by the global anticorrelation between dispersion and intensity [e.g., Bogue and Coe, 1984; Love, 2000]. When latitudinal averages for global paleointensity estimates for the past 5 Ma are plotted there is no sign of the expected increase with latitude due to a dipole field. One plausible explanation for this is temporal sampling bias in a (dipolar) field of time varying magnitude. However,

it seems unlikely that this can fully explain the persistent low intensity at McMurdo during relatively well-sampled time periods. While these paleomagnetic data cannot provide direct dynamical constraints on features like polar vortices inside the tangent cylinder, they will provide useful constraints on statistical models for PSV. In conjunction with theoretical studies of numerical dynamo simulations, future studies may lead to greater insight about tangent cylinder field dynamics.

Acknowledgments

[58] We thank Julie Bowles, Jasper Konter, and Elise Sbarbori for their hard work in the field collecting the new samples presented in this paper, as well as E.A. Mankinen for the previously collected samples. We thank Jason Steindorf for his contributions in sample preparation and processing. We are grateful to Frank Vernon, Mert Ingraham, and Mark Zumberge for their assistance in developing the GPS orientation method. We thank Jean Pierre Valet, Robert Coe, Brad Singer, and Masaru Kono for their insightful reviews, which have improved this manuscript. This research was supported by NSF grants 0538392 and 0229403.

References

- Aurnou, J., S. Andreadis, L. Zhu, and P. Olson (2003), Experiments on convection in Earth's core tangent cylinder, *Earth Planet. Sci. Lett.*, *212*(1–2), 119–134, doi:10.1016/S0012-821X(03)00237-1.
- Baraldo, A., A. E. Rapalini, H. Bohnel, and M. Mena (2003), Paleomagnetic study of Deception Island, South Shetland Islands, Antarctica, *Geophys. J. Int.*, *153*, 333–343, doi:10.1046/j.1365-246X.2003.01881.x.
- Ben-Yosef, E., H. Ron, L. Tauxe, A. Agnon, A. Genevey, T. E. Levy, U. Avner, and M. Najjar (2008), Application of copper slag in archeointensity research, *J. Geophys. Res.*, *113*, B08101, doi:10.1029/2007JB005235.
- Biggin, A. J., G. H. M. A. Strik, and C. G. Langereis (2008), The intensity of the geomagnetic field in the late-Archaeon: New measurements and an analysis of the updated IAGA palaeointensity database, *Earth Planets Space*, in press.
- Bloxham, J., and A. Jackson (1992), Time-dependent mapping of the magnetic-field at the core-mantle boundary, *J. Geophys. Res.*, *97*(B13), 19,537–19,563, doi:10.1029/92JB01591.
- Bloxham, J., D. Gubbins, and A. Jackson (1989), Geomagnetic secular variation, *Philos. Trans. R. Soc. London, Ser. A*, *329*(1606), 415–502.
- Bogue, S., and R. S. Coe (1984), Transitional paleointensities from Kauai, Hawaii, and geomagnetic reversal models, *J. Geophys. Res.*, *89*(12), 10,341–10,354.
- Cande, S. C., J. M. Stock, R. D. Muller, and I. Takemi (2000), Cenozoic motion between East and West Antarctica, *Nature*, *404*, 145–150, doi:10.1038/35004501.
- Carlut, J., X. Quidelleur, V. Courtillot, and G. Boudon (2000), Paleomagnetic directions and K/Ar dating of 0 to 1 Ma lava flows from La Guadeloupe Island (French West Indies): Implications for time-averaged field models, *J. Geophys. Res.*, *105*(B1), 835–849, doi:10.1029/1999JB900238.
- Christensen, U. R., and J. Wicht (2007), Numerical dynamo simulations, in *Treatise on Geophysics, Core Dynamics*, edited by P. Olson, pp. 245–282, Elsevier, New York.
- Christensen, U. R., P. Olson, and G. A. Glatzmaier (1998), A dynamo model interpretation of geomagnetic field structures, *Geophys. Res. Lett.*, *25*, 1565–1568, doi:10.1029/98GL00911.
- Clement, B. M. (2000), Assessing the fidelity of palaeomagnetic records of geomagnetic reversal, *Philos. Trans. R. Soc. London*, *358*(1768), 1049–1064.
- Coe, R. S., S. Gromme, and E. A. Mankinen (1978), Geomagnetic paleointensities from radiocarbon-dated lava flows on Hawaii and the question of the Pacific nondipole low, *J. Geophys. Res.*, *83*, 1740–1756, doi:10.1029/JB083iB04p01740.
- Coe, R. S., L. Hongre, and G. A. Glatzmaier (2000), An examination of simulated geomagnetic reversals from a palaeomagnetic perspective, *Philos. Trans. R. Soc. London*, *358*(1768), 1141–1170.
- Constable, C. G., and C. L. Johnson (2005), A paleomagnetic power spectrum, *Phys. Earth Planet. Inter.*, *153*(1–3), 61–73, doi:10.1016/j.pepi.2005.03.015.
- Constable, C. G., and R. L. Parker (1988), Statistics of the geomagnetic secular variation for the past 5 m.y., *J. Geophys. Res.*, *93*, 11,569–11,581, doi:10.1029/JB093iB10p11569.
- Creer, K. M. (1962), The dispersion of the geomagnetic field due to secular variation and its determination from remote times from paleomagnetic data, *J. Geophys. Res.*, *67*, 3461–3476, doi:10.1029/JZ067i009p03461.
- Esser, R. P., P. R. Kyle, and W. C. McIntosh (2004), ⁴⁰Ar/³⁹Ar dating of the eruptive history of Mount Erebus, Antarctica: Volcano evolution, *Bull. Volcanol.*, *66*, 671–686, doi:10.1007/s00445-004-0354-x.
- Fisher, R. A. (1953), Dispersion on a sphere, *Proc. R. Soc. London, Ser. A*, *217*, 295–305, doi:10.1098/rspa.1953.0064.
- Fitzgerald, P. (2002), Tectonics and landscape evolution of the Antarctic plate since the break-up of Gondwana, with an emphasis on the West Antarctic Rift System and the Transantarctic Mountains, *Bull. R. Soc. N. Z.*, *35*, 453–469.
- Glatzmaier, G. A., R. S. Coe, L. Hongre, and P. H. Roberts (1999), The role of the Earth's mantle in controlling the frequency of geomagnetic reversals, *Nature*, *401*, 885–890, doi:10.1038/44776.
- Gubbins, D., A. L. Jones, and C. C. Finlay (2006), Fall in the Earth's magnetic field and implications for the geodynamo, *Science*, *312*, 900–902, doi:10.1126/science.1124855.
- Harrington, H. J. (1958), Nomenclature of rock units in the Ross Sea region, Antarctica, *Nature*, *182*(4631), 290, doi:10.1038/182290a0.
- Harrison, R. J., and J. M. Feinberg (2008), FORCinel: An improved algorithm for calculating first-order reversal curve distributions using locally weighted regression smoothing, *Geochem. Geophys. Geosyst.*, *9*, Q05016, doi:10.1029/2008GC001987.
- Herrero-Bervera, E., and R. S. Coe (1999), Transitional field behavior during the Gilbert-Gauss and Lower Mammoth reversals recorded in lavas from the Wai'anae volcano, O'ahu, Hawaii, *J. Geophys. Res.*, *104*(B12), 29,157–29,173.
- Herrero-Bervera, E., and J.-P. Valet (2005), Absolute paleointensity and reversal records from the Waianae sequence (Oahu, Hawaii, USA), *Earth Planet. Sci. Lett.*, *234*(1–2), 279–296, doi:10.1016/j.epsl.2005.02.032.
- Holt, J. W., J. L. Kirschvink, and F. Garnier (1996), Geomagnetic field inclinations for the past 400 kyr from the 1-km core of the Hawaii Scientific Drilling Project, *J. Geophys. Res.*, *101*(B5), 11,655–11,663, doi:10.1029/95JB03843.

- Hulot, G., C. Eymin, B. Langlais, M. Mandea, and N. Olsen (2002), Small-scale structure of the geodynamo inferred from Oersted and Magsat satellite data, *Nature*, *416*(6881), 620–623, doi:10.1038/416620a.
- Jackson, A., A. R. T. Jonkers, and M. R. Walker (2000), Four centuries of geomagnetic secular variation from historical records, *Philos. Trans. R. Soc. London, Ser. A*, *358*(1768), 957–990.
- Johnson, C. L. (2008), Recent investigations of the 0–5 Ma geomagnetic field recorded by lava flows, *Geochem. Geophys. Geosyst.*, *9*, Q04030, doi:10.1029/2007GC001719.
- Johnson, C. L., and P. L. McFadden (2007), The time-averaged field and paleosecular variation, in *Treatise on Geophysics, Geomagnetism Volume*, edited by M. Kono, pp. 417–453, Elsevier, New York.
- Johnson, C. L., J. R. Wijbrans, C. G. Constable, J. Gee, H. Staudigel, L. Tauxe, V.-H. Forjaz, and M. Salgueiro (1998), $^{40}\text{Ar}/^{39}\text{Ar}$ Ages and paleomagnetism of Sao Miguel lavas, Azores, *Earth Planet. Sci. Lett.*, *160*, 637–649, doi:10.1016/S0012-821X(98)00117-4.
- Jovane, L., G. Acton, F. Florindo, and K. Verosub (2008), Geomagnetic field behavior at high latitudes from a paleomagnetic record from Eltanin core 27–21 in the Ross Sea sector, *Antarctica, Earth Planet. Sci. Lett.*, *267*, 435–443, doi:10.1016/j.epsl.2007.12.006.
- Kirschvink, J. L. (1980), The least-squares line and plane and the analysis of paleomagnetic data, *Geophys. J. R. Astron. Soc.*, *62*, 699–718.
- Kono, M., and P. H. Roberts (2002), Recent geodynamo simulations and observations of the geomagnetic field, *Rev. Geophys.*, *40*(4), 1013, doi:10.1029/2000RG000102.
- Kono, M., A. Sakuraba, and M. Ishida (2000), Dynamo simulation and palaeosecular variation models, *Philos. Trans. R. Soc. London, Ser. A*, *358*, 1123–1139.
- Korte, M., and C. G. Constable (2005), Continuous geomagnetic field models for the past 7 millennia: 2. CALS7K, *Geochem. Geophys. Geosyst.*, *6*, Q02H16, doi:10.1029/2004GC000801.
- Kyle, P. R. (1981), Glacial history of the McMurdo Sound area as indicated by the distribution and nature of McMurdo Volcanic Group rocks, in *Dry Valley Drilling Project, Antarct. Res. Ser.*, vol. 33, edited by L. D. McGinnis, pp. 403–412, AGU, Washington, D. C.
- Kyle, P. R. (1990a), Erebus Volcanic Province: Summary, in *Volcanoes of the Antarctic Plate and Southern Oceans, Antarct. Res. Ser.*, vol. 48, edited by W. LaMasurier and J. Thomson, pp. 81–88, AGU, Washington, D. C.
- Kyle, P. R. (1990b), McMurdo Volcanic Group-Western Ross Embayment: Introduction, in *Volcanoes of the Antarctic Plate and Southern Oceans, Antarct. Res. Ser.*, vol. 48, edited by W. LaMasurier and J. Thomson, pp. 18–25, AGU, Washington, D. C.
- Kyle, P. R., and J. W. Cole (1974), Structural control of volcanism in the McMurdo Volcanic Group, Antarctica, *Bull. Volcanol.*, *38*(1), 16–25, doi:10.1007/BF02597798.
- Laj, C., C. Kissel, V. Scao, J. Beer, D. M. Thomas, H. Guillou, R. Muscheler, and G. Wagner (2002), Geomagnetic intensity and inclination variations at Hawaii for the past 98 kyr from core SOH-4 (Big Island): A New study and a comparison with existing contemporary data, *Phys. Earth Planet. Inter.*, *129*, 205–243, doi:10.1016/S0031-9201(01)00291-6.
- Love, J. J. (2000), On the anisotropy of secular variation deduced from paleomagnetic volcanic data, *J. Geophys. Res.*, *105*, 5799–5816, doi:10.1029/1999JB900395.
- Macouin, M., J. P. Valet, J. Besse, and R. E. Ernst (2006), Absolute paleointensity at 1.27 Ga from the Mackenzie dyke swarm (Canada), *Geochem. Geophys. Geosyst.*, *7*, Q01H21, doi:10.1029/2005GC000960.
- Macri, P., L. Sagnotti, J. Dinares-Turell, and A. Caburlotto (2005), A composite record of Pleistocene relative geomagnetic paleointensity from Wilkes Land Basin (Antarctica), *Phys. Earth Planet. Inter.*, *151*, 223–242, doi:10.1016/j.pepi.2005.03.004.
- Macri, P., L. Sagnotti, R. G. Lucchi, and M. Rebesco (2006), A stacked record of relative geomagnetic paleointensity for the past 270 kyr from the western continental rise of the Antarctic Peninsula, *Earth Planet. Sci. Lett.*, *252*(1–2), 162–179, doi:10.1016/j.epsl.2006.09.037.
- Mankinen, E. A., and A. Cox (1988), Paleomagnetic investigation of some volcanic rocks from the McMurdo volcanic province, Antarctica, *J. Geophys. Res.*, *93*, 11,599–11,612, doi:10.1029/JB093iB10p11599.
- McElhinny, M. W., P. L. McFadden, and R. T. Merrill (1996), The time-averaged paleomagnetic field 0–5 Ma, *J. Geophys. Res.*, *101*(B11), 25,007–25,028, doi:10.1029/96JB01911.
- McFadden, P. L., and M. W. McElhinny (1988), The combined analysis of remagnetization circles and direct observations in palaeomagnetism, *Earth Planet. Sci. Lett.*, *87*(1–2), 161–172, doi:10.1016/0012-821X(88)90072-6.
- McFadden, P. L., R. T. Merrill, and M. W. McElhinny (1988), Dipole/quadrupole family modeling of paleosecular variation, *J. Geophys. Res.*, *93*, 11,583–11,588, doi:10.1029/JB093iB10p11583.
- Mejia, V., H. Bohnel, N. Opdyke, M. A. Ortega-Rivera, J. K. W. Lee, and J. J. Aranda-Gomez (2005), Paleosecular variation and time-averaged field recorded in late-Pliocene-Holocene lava flows from Mexico, *Geochem. Geophys. Geosyst.*, *6*, Q07H19, doi:10.1029/2004GC000871.
- Miki, M., H. Inokuchi, S. Yamaguchi, J.-i. Matsuda, K. Nagao, N. Isezaki, and K. Yaskawa (1998), Geomagnetic paleosecular variation in Easter Island, the southeast Pacific, *Phys. Earth Planet. Inter.*, *106*, 93–101, doi:10.1016/S0031-9201(97)00106-4.
- Olson, P., and J. Aurnou (1999), A polar vortex in the Earth's core, *Nature*, *402*(6758), 170–173, doi:10.1038/46017.
- Pick, T., and L. Tauxe (1993), Holocene Paleointensities: Thellier experiments on submarine basaltic glass from the east Pacific Rise, *J. Geophys. Res.*, *98*(B10), 17,949–17,964, doi:10.1029/93JB01160.
- Renne, P. R., C. C. Swisher, A. L. Deino, D. B. Karner, T. L. Owens, and D. J. DePaolo (1998), Intercalibration of standards, absolute ages and uncertainties in $^{40}\text{Ar}/^{39}\text{Ar}$ dating, *Chem. Geol.*, *145*(1–2), 117–152, doi:10.1016/S0009-2541(97)00159-9.
- Riisager, P., and J. Riisager (2001), Detecting multidomain magnetic grains in the Thellier palaeointensity experiments, *Phys. Earth Planet. Inter.*, *125*(1–4), 111–117, doi:10.1016/S0031-9201(01)00236-9.
- Roberts, A. P., A. Bakrania, F. Florindo, C. J. Rowan, C. R. Fielding, and R. D. Powell (2007), High-resolution evidence for dynamic transitional geomagnetic behaviour from a Miocene reversal, McMurdo Sound, Ross Sea, Antarctica, *Earth Planets Space*, *59*, 815–824.
- Sakuraba, A., and M. Kono (1999), Effect of the inner core on the numerical solution of the magnetohydrodynamic dynamo, *Phys. Earth Planet. Inter.*, *111*, 105–121, doi:10.1016/S0031-9201(98)00150-2.
- Selkin, P. A., J. S. Gee, L. Tauxe, W. P. Meurer, and A. J. Newell (2000), The effect of remanence anisotropy on paleointensity estimates; a case study from the Archean Stillwater Complex, *Earth Planet. Sci. Lett.*, *183*(3–4), 403–416, doi:10.1016/S0012-821X(00)00292-2.

- Selkin, P. A., J. Gee, and L. Tauxe (2007), Nonlinear thermoremanence acquisition and implications for paleointensity data, *Earth Planet. Sci. Lett.*, *256*(1–2), 81–89, doi:10.1016/j.epsl.2007.01.017.
- Sreenivasan, B., and C. A. Jones (2005), Structure and dynamics of the polar vortex in the Earth's core, *Geophys. Res. Lett.*, *32*, L20301, doi:10.1029/2005GL023841.
- Sreenivasan, B., and C. A. Jones (2006), Azimuthal winds, convection and dynamo action in the polar regions of planetary cores, *Geophys. Astrophys. Fluid Dyn.*, *100*(4–5), 319–339, doi:10.1080/03091920600807864.
- Steiger, R. H., and E. Jäger (1977), Subcommittee on geochronology: Convention on the use of decay constants in geo- and cosmochronology, *Earth Planet. Sci. Lett.*, *36*, 359–362, doi:10.1016/0012-821X(77)90060-7.
- Stephenson, A. (1993), 3-Axis static alternating-field demagnetization of rocks and the identification of natural remanent magnetization, gyroremanent magnetization, and anisotropy, *J. Geophys. Res.*, *98*(B1), 373–381, doi:10.1029/92JB01849.
- Takahashi, F., M. Matsushima, and Y. Honkura (2008), Scale variability in convection-driven MHD dynamos at low Ekman numbers, *Phys. Earth Planet. Inter.*, *167*(3–4), 168–178, doi:10.1016/j.pepi.2008.03.005.
- Tauxe, L., and D. V. Kent (2004), A simplified statistical model for the geomagnetic field and the detection of shallow bias in paleomagnetic inclinations: Was the ancient magnetic field dipolar?, in *Timescales of the Paleomagnetic Field*, *Geophys. Monogr. Ser.*, vol. 145, edited by J. E. T. Channell et al., 320 pp., AGU, Washington, D. C.
- Tauxe, L. T., and H. Staudigel (2004), Strength of the geomagnetic field in the Cretaceous Normal Superchron: New data from submarine basaltic glass of the Troodos Ophiolite, *Geochem. Geophys. Geosyst.*, *5*, Q02H06, doi:10.1029/2003GC000635.
- Tauxe, L., and T. Yamazaki (2007), Paleointensities, in *Treatise on Geophysics*, vol. 5, edited by M. Kono, pp. 509–563, Elsevier, New York.
- Tauxe, L., T. A. T. Mullender, and T. Pick (1996), Potbellies, wasp-waists and superparamagnetism in magnetic hysteresis, *J. Geophys. Res.*, *101*, 571–583, doi:10.1029/95JB03041.
- Tauxe, L., H. Staudigel, and J. R. Wijbrans (2000), Paleomagnetism and $^{40}\text{Ar}/^{39}\text{Ar}$ ages from La Palma in the Canary Islands, *Geochem. Geophys. Geosyst.*, *1*(9), 1038, doi:10.1029/2000GC000063.
- Tauxe, L., C. G. Constable, C. L. Johnson, A. A. P. Koppers, W. R. Miller, and H. Staudigel (2003), Paleomagnetism of the southwestern U.S.A. recorded by 0–5 Ma igneous rocks, *Geochem. Geophys. Geosyst.*, *4*(4), 8802, doi:10.1029/2002GC000343.
- Tauxe, L., P. Gans, and E. A. Mankinen (2004a), Paleomagnetism and $^{40}\text{Ar}/^{39}\text{Ar}$ ages from volcanics extruded during the Matuyama and Brunhes chrons near McMurdo Sound, Antarctica, *Geochem. Geophys. Geosyst.*, *5*, Q06H12, doi:10.1029/2003GC000656.
- Tauxe, L., C. Luskin, P. A. Selkin, P. Gans, and A. Calvert (2004b), Paleomagnetic results from the Snake River Plain: Contribution to the time-averaged field global database, *Geochem. Geophys. Geosyst.*, *5*, Q08H13, doi:10.1029/2003GC000661.
- Taylor, J. R. (1982), *An Introduction to Error Analysis: The Study of Uncertainties in Physical Measurements*, 270 pp., Univ. Sci. Books, Mill Valley, Calif.
- Thellier, E., and O. Thellier (1959), Sur l'intensité du champ magnétique terrestre dans le passé historique et géologique, *Ann. Geophys.*, *15*, 285–378.
- Valet, J. P., L. Meynadier, and Y. Guyodo (2005), Geomagnetic dipole strength and reversal rate over the past two million years, *Nature*, *435*(7043), 802–805, doi:10.1038/nature03674.
- Vandamme, D. (1994), A new method to determine paleosecular variation, *Phys. Earth Planet. Inter.*, *85*, 131–142, doi:10.1016/0031-9201(94)90012-4.
- Wardinski, L., and R. Holme (2006), A time-dependent model of the Earth's magnetic field and its secular variation for the period 1980–2000, *J. Geophys. Res.*, *111*, B12101, doi:10.1029/2006JB004401.
- Wilch, T. I. (1991), The surficial geology and geochronology of middle Taylor Valley Antarctica: Implications for Pliocene-Pleistocene Antarctic glacial history, M.S. thesis, Univ. of Maine, Orono.
- Wilch, T. I., D. R. Lux, G. H. Denton, and W. C. McIntosh (1993), Minimal Pliocene-Pleistocene uplift of the dry valleys sector of the Transantarctic Mountains: A key parameter in ice-sheet reconstructions, *Geology*, *21*, 841–844, doi:10.1130/0091-7613(1993)021<0841:MPPUOT>2.3.CO;2.
- York, D. (1969), Least squares fitting of a straight line with correlated errors, *Earth Planet. Sci. Lett.*, *5*(5), 320–324.
- Yu, Y. J., L. T. Tauxe, and A. Genevey (2004), Toward an optimal geomagnetic field intensity determination technique, *Geochem. Geophys. Geosyst.*, *5*, Q02H07, doi:10.1029/2003GC000630.
- Ziegler, L. B., C. G. Constable, and C. L. Johnson (2008), Testing the robustness and limitations of 0–1 Ma absolute paleointensity data, *Phys. Earth Planet. Inter.*, *170*, 34–45, doi:10.1016/j.pepi.2008.1007.1027.